Article

Molecular Cell

Lipid Droplet-Derived Monounsaturated Fatty Acids Traffic via PLIN5 to Allosterically Activate SIRT1

Graphical Abstract

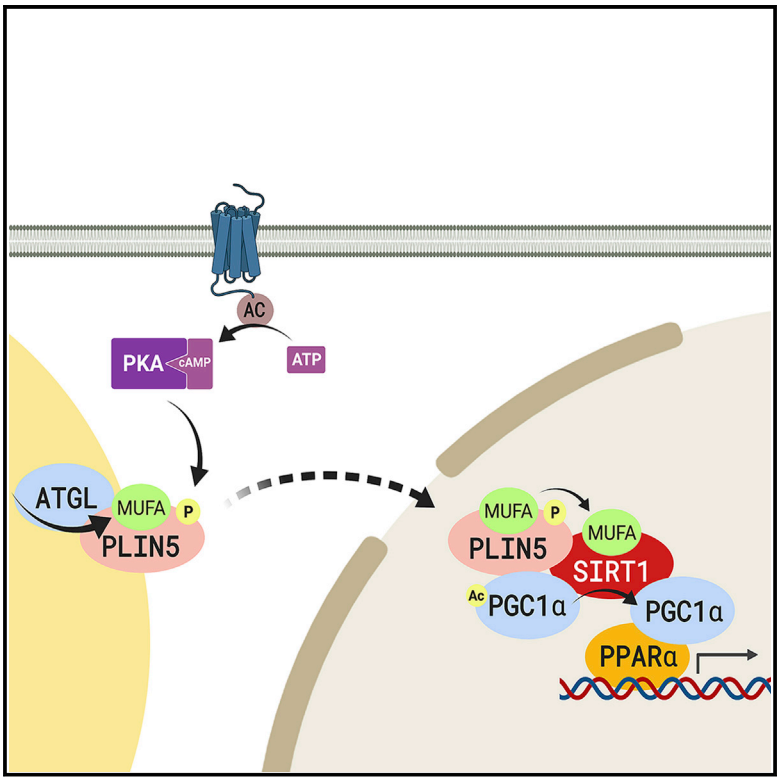

Authors

Charles P. Najt, Salmaan A. Khan, Timothy D. Heden, ..., Laurie Parker, Lisa S. Chow, Douglas G. Mashek

Correspondence

dmashek@umn.edu

In Brief

Najt et al. identify the first-known endogenous allosteric modulator of SIRT1 and characterize a lipid droplet-nuclear signaling axis that underlies the known metabolic benefits of monounsaturated fatty acids and PLIN5.

Highlights

- MUFAs allosterically activate SIRT1 toward select substrates such as PGC-1α
- MUFAs enhance PGC-1α signaling *in vivo* in a SIRT1-dependent manner
- PLIN5 is a fatty acid binding protein that preferentially binds LD-derived MUFAs
- PLIN5 mediates MUFA signaling to control SIRT1/PGC-1α

Najt et al., 2020, Molecular Cell 77, 810–824
February 20, 2020 © 2019 Elsevier Inc.
https://doi.org/10.1016/j.molcel.2019.12.003

CellPress

CellPress

Molecular Cell
Article

Lipid Droplet-Derived Monounsaturated Fatty Acids Traffic via PLIN5 to Allosterically Activate SIRT1

Charles P. Najt,[1] Salmaan A. Khan,[1] Timothy D. Heden,[1] Bruce A. Witthuhn,[1] Minervo Perez,[1] Jason L. Heier,[1] Linnea E. Mead,[1] Mallory P. Franklin,[2] Kenneth K. Karanja,[1] Mark J. Graham,[3] Mara T. Mashek,[1] David A. Bernlohr,[1] Laurie Parker,[1] Lisa S. Chow,[4] and Douglas G. Mashek[1,4,5,*]

[1]Department of Biochemistry, Molecular Biology and Biophysics, University of Minnesota, Minneapolis, MN, USA
[2]Department of Food Science and Nutrition, University of Minnesota, Minneapolis, MN, USA
[3]Ionis Pharmaceuticals, Inc., Carlsbad, CA, USA
[4]Department of Medicine, Division of Diabetes, Endocrinology and Metabolism, University of Minnesota, Minneapolis, Minnesota, USA
[5]Lead Contact
*Correspondence: dmashek@umn.edu
https://doi.org/10.1016/j.molcel.2019.12.003

SUMMARY

Lipid droplets (LDs) provide a reservoir for triacylglycerol storage and are a central hub for fatty acid trafficking and signaling in cells. Lipolysis promotes mitochondrial biogenesis and oxidative metabolism via a SIRT1/PGC-1α/PPARα-dependent pathway through an unknown mechanism. Herein, we identify that monounsaturated fatty acids (MUFAs) allosterically activate SIRT1 toward select peptide-substrates such as PGC-1α. MUFAs enhance PGC-1α/PPARα signaling and promote oxidative metabolism in cells and animal models in a SIRT1-dependent manner. Moreover, we characterize the LD protein perilipin 5 (PLIN5), which is known to enhance mitochondrial biogenesis and function, to be a fatty-acid-binding protein that preferentially binds LD-derived monounsaturated fatty acids and traffics them to the nucleus following cAMP/PKA-mediated lipolytic stimulation. Thus, these studies identify the first-known endogenous allosteric modulators of SIRT1 and characterize a LD-nuclear signaling axis that underlies the known metabolic benefits of MUFAs and PLIN5.

INTRODUCTION

During increased energy demand, fatty acids are hydrolyzed from triacylglycerol stored in cytoplasmic LDs to provide substrates for β-oxidation and oxidative phosphorylation. The hydrolysis of triacylglycerols (i.e., lipolysis) via adipose triglyceride lipase (ATGL), the major triacylglycerol lipase in most tissues, promotes the activation of the transcription factor and co-activator complex of PPAR-α/PGC-1α to upregulate mitochondrial biogenesis and, thus, couple oxidative capacity with the supply of fatty acid substrates (Haemmerle et al., 2011; Khan et al., 2015; Ong et al., 2011). While the supply of fatty acid ligands to activate PPAR-α may contribute to these effects (Haemmerle et al., 2011), we have shown that sirtuin 1 (SIRT1), which is known to deacetylate PGC-1α and promote its interaction with transcription partners, is activated in response to ATGL-catalyzed lipolysis and is required for ATGL-mediated upregulation of PPAR-α/PGC-1α signaling (Khan et al., 2015). Moreover, cAMP/PKA signaling, which promotes lipolysis and SIRT1, requires ATGL-catalyzed lipolysis for the induction of SIRT1 activity, suggesting that ATGL is a key upstream regulator of SIRT1. A member of the sirtuin family of NAD^+-dependent protein deacetylases, SIRT1 has a wide-range of biological functions including chromatin structure maintenance, cell cycle control, metabolism, and the regulation of healthspan (Banks et al., 2008; Bordone et al., 2007; Houtkooper et al., 2012; Pfluger et al., 2008). In mice, SIRT1 promotes characteristics reminiscent of caloric restriction such as a decrease in the incidence of age-related diseases including diabetes, cardiovascular disorders, and neurodegenerative diseases (Balasubramanian et al., 2017; Banks et al., 2008; Bordone et al., 2007; Chen et al., 2005; Pfluger et al., 2008). Numerous dietary small molecule activators of SIRT1, such as the polyphenol resveratrol and related compounds, have been identified and used to attenuate aging-related disease and improve lifespan (Hubbard and Sinclair, 2014; Kim et al., 2007; Lagouge et al., 2006; Sinclair and Guarente, 2014). Thus, SIRT1 plays a key role in sensing intracellular redox (i.e., NAD) and dietary phytochemicals to coordinate cellular function and disease resistance.

LD accumulation in non-adipose tissue is a hallmark and etiological factor of numerous diseases (Greenberg et al., 2011). Increased LDs in cells is commonly associated with lipotoxicity and altered metabolism that contributes to cellular dysfunction. Perilipin 5, a member of the perilipin (PLIN) family of LD proteins has been positively correlated with both triacylglycerol storage and fatty acid oxidation and uncouples LD accumulation from lipotoxicity and metabolic dysfunction (Dalen et al., 2007; Gemmink et al., 2016; Kuramoto et al., 2012; Mohktar et al., 2016; Pollak et al., 2015; Wang et al., 2015; Wolins et al., 2006). Under basal conditions, PLIN5 directly interacts with and inhibits ATGL, but in response to lipolytic stimuli, such as cAMP/PKA signaling, it promotes triacylglycerol hydrolysis and fatty acid oxidation (Granneman et al., 2009, 2011; Wang et al., 2015). While gain-and-loss of function studies have shown a connection between

PLIN5 and fatty acid metabolism, the mechanism by which PLIN5 contributes to oxidative metabolism has remained largely unknown. Recent work providing insights into this mechanism demonstrate that PLIN5 interacts with PGC-1α and SIRT1 to promote PGC-1α/PPAR-α activity (Gallardo-Montejano et al., 2016).

Given that both ATGL and PLIN5 have been linked to SIRT1, we sought to elucidate the interplay between these two LD proteins and the mechanisms through which ATGL-mediated lipolysis promotes SIRT1 activity and downstream PGC-1α/PPAR-α signaling. Herein, we show that a specific class of fatty acids, MUFAs, bind and allosterically activate SIRT1 by reducing its K_m for select peptide substrates. In addition, we identify PLIN5 to be a fatty acid binding protein that preferentially binds MUFAs derived from ATGL-catalyzed lipolysis and shuttles them to the nucleus for activation of SIRT1 following lipolytic stimulation.

RESULTS

MUFAs Are Allosteric Activators of SIRT1 at Nanomolar Concentrations

Given that ATGL promotes SIRT1 signaling, we explored if the products of ATGL-catalyzed lipolysis, fatty acids, could activate SIRT1. Indeed, SIRT1 has a hydrophobic pocket thought to be responsible for binding resveratrol and related sirtuin-activating compounds (Borra et al., 2005; Cao et al., 2015; Kaeberlein et al., 2005). Using an MS-based selected reaction monitoring method with recombinant SIRT1 (Figures S1A–S1C), we found that the kinetics of PGC-1α peptide deacetylation were altered in the presence of the fatty acid 18:1 (Figures 1A–1D). The increase in SIRT1 catalytic efficiency (K_{cat}/K_m) was due to a lowering of the K_m of SIRT1 toward the PGC-1α peptide without a significant change in enzyme velocity. This effect was not additive to resveratrol, as co-addition of 18:1 and resveratrol did not alter the K_m or catalytic efficiency when compared to addition of a single lipophilic compound (Figures 1E and 1F), suggesting that 18:1 and resveratrol may activate SIRT1 through a common binding site. We next explored if other fatty acids had similar effects on SIRT1. While 17:1, 16:0, and 18:0 were unable to stimulate SIRT1 deacetylase activity, the addition of 16:1 also resulted in a lowering of the K_m and an increase in catalytic efficiency toward the PGC-1α peptide comparable to the effects observed with 18:1 (Figures 1G and 1H). For both even chain MUFAs, activation of SIRT1 was seen at concentrations of fatty acids ranging from 150 nM to 1 μM, but no deacetylase activation was observed at concentrations above 1 μM (Figures 1D–1H).

Next, we determined if fatty acid activation of SIRT1 was due to direct binding. Using tryptophan quenching assays, saturable binding curves for 18:1 and 16:1 were observed with K_d values of 81 ± 9 nM, and 100 ± 3 nM, respectively (Figures 1I and 1J). No fatty acid binding was observed for 18:0, 16:0, or trans-18:1 (Figure 1K), suggesting a preference for cis-MUFAs. To further support these findings, fluorescence binding and displacement assays using 1,8-ANS were performed (Kane and Bernlohr, 1996). Displacement of the bound fluorophore using 18:1, 16:1, or resveratrol as a competing ligand revealed K_i values of 5.6 ± 0.12, 12.5 ± 0.06, and 16.7 ± 0.07 μM, respectively; displacement of 1,8-ANS was not observed with 18:0 and 16:0 (Figure 1L; Table S1). Structure analysis using CD revealed that MUFAs elicited large changes in secondary structure with increased α−helical content of SIRT1 from 23% to 25.9% and 23% to 28.6% for 16:1 and 18:1, respectively (Figure S1D; Table S2). The addition of 16:0 and 18:0 did not alter the shape of the CD spectrum of SIRT1 consistent with the lack of tryptophan quenching and ANS displacement showing no binding. These results suggest that MUFA-mediated allosteric activation of SIRT1 was due to direct fatty acid binding and subsequent conformational changes to the enzyme.

The activation of SIRT1 in response to resveratrol and related compounds is highly selective based upon the peptide substrate (Hubbard et al., 2013). Therefore, we tested if the ability of MUFAs to activate SIRT1 is also influenced by the acetyl peptide sequence. We chose peptide sequences from established SIRT1 targets FOXO3a and H3 (Figure S1A). Similar to the results obtained with PGC-1α, 18:1 also increased SIRT1 activity toward the FOXO3a peptide through a reduced K_m and increased catalytic efficiency comparable to what was observed with 10 μM resveratrol (Figures 2A–2F). In contrast, MUFAs were unable to increase SIRT1 activity toward the H3 peptide substrate (Figures 2G–2K). In fact, MUFA concentrations of 600 nM or more increased the K_m and decreased K_{cat}/K_m, indicating inhibitory effects toward the H3 peptide. To further explore substrate selectivity, we used a competition assay with fixed amounts of PGC-1α, FOXO3a, and H3 peptides and two doses of 18:1. The addition of either 150 or 600 nM 18:1 increased deacetylase activity toward FOXO3a and PGC-1α peptides, but decreased activity toward H3 (Figure 2L). Taken together, these data show that MUFAs selectively target SIRT1 to specific peptide substrates.

A hydrophobic residue at the +1 or +6 position upstream of the acetylated lysine is required for allosteric activation of SIRT1 (Hubbard et al., 2013). To determine if a similar requirement exists for MUFA activation, SIRT1 activity toward a p53 peptide was determined (Figures S1A, S2A, and S2B). Lacking a hydrophobic residue at the +1 or +6 position resulted in a SIRT1 substrate that did not respond to allosteric activation via 18:1, resveratrol, or the SIRT1 activating compound SRT1720 (Figures S2A and S2B). In contrast to the wild-type p53 peptide substrate, a mutant p53 peptide (p53-W) containing a tryptophan at the +6 position in replacement of alanine was activated in response to 250 nM 18:1, 10 μM resveratrol, and 1 μM SRT1720 (Figures S2C–S2G). Examining the PGC-1α, FOXO3a, and the H3 peptide substrates, both the PGC-1α and the FOXO3a substrates contained a hydrophobic residue at the +1 position, valine for PGC-1α and tryptophan for FOXO3a, while the H3 substrate did not (Figure S1A). Taken together, these data show that MUFAs selectively target SIRT1 to specific peptide substrates through the positioning of hydrophobic residues at either the +1 or the +6 position relative to the acetylated lysine, similar to what has been reported for resveratrol and SRT1720.

18:1 Increases PGC-1α Transcriptional Activity in a SIRT1-Dependent Manner

Since MUFAs bind and allosterically activate SIRT1, we tested the effects of lipolysis-derived 18:1 on SIRT1/PGC-1α signaling.

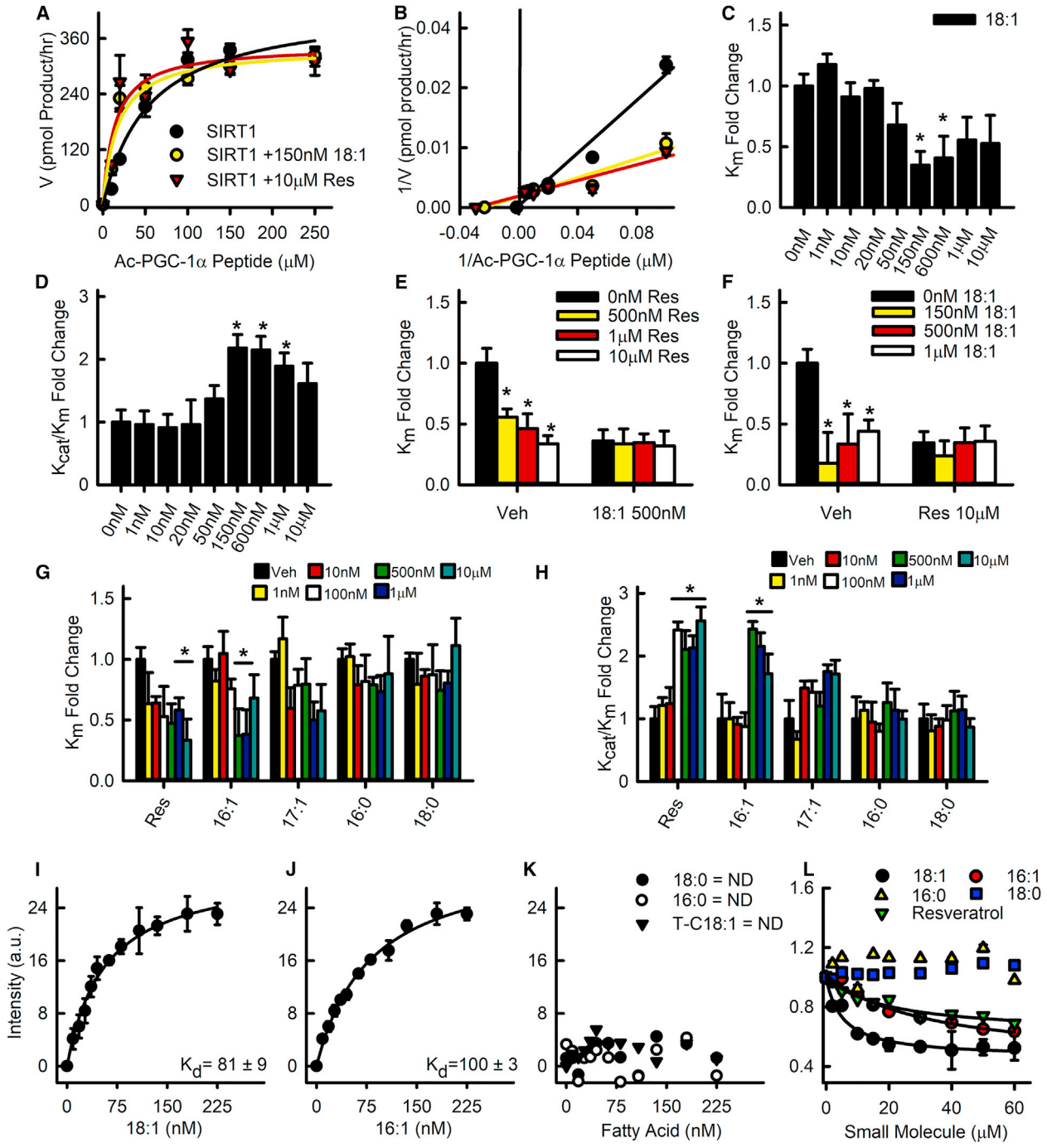

Figure 1. The MUFAs 18:1 and 16:1 Allosterically Activate SIRT1 toward a PGC-1α Substrate

(A) Saturation plot of the effect of fatty acids and resveratrol (Res) on human SIRT1 enzyme activity was measured by mass spectrometry (see STAR Methods) using a native peptide sequence of acetylated-PGC-1α. Data represent the mean ± SEM from quadruplicate experiments.

(B) Lineweaver-Burk reciprocal plots were generated to determine K_m, V_{max}, and K_{cat}. Data represent the mean ± SEM from quadruplicate experiments.

(C and D) K_m (C) and K_{cat}/K_m (D) fold change for each concentration of 18:1. Data represent the mean ± SEM from quadruplicate experiments. * $p < 0.05$.

(E and F) Competition assays between 18:1 (E) and resveratrol (F). Data represent the mean ± SEM from quadruplicate experiments. * $p < 0.05$.

(G and H) K_m (G) and K_{cat}/K_m (H) fold change for each concentration of resveratrol and long chain fatty acids. Data represent the mean ± SEM from quadruplicate experiments. * $p < 0.05$.

(I–K) SIRT1 binding affinity for fatty acids was determined by tryptophan fluorescence quenching assay with 18:1 (I), 16:1 (J) or other long chain fatty acids (K); (ND = not detected). Data represent the mean ± SEM from triplicate experiments.

(L) Displacement of 1,8-ANS was used to determine the K_i of SIRT1 for fatty acids and resveratrol. Data represent the mean ± SEM from n = 6.

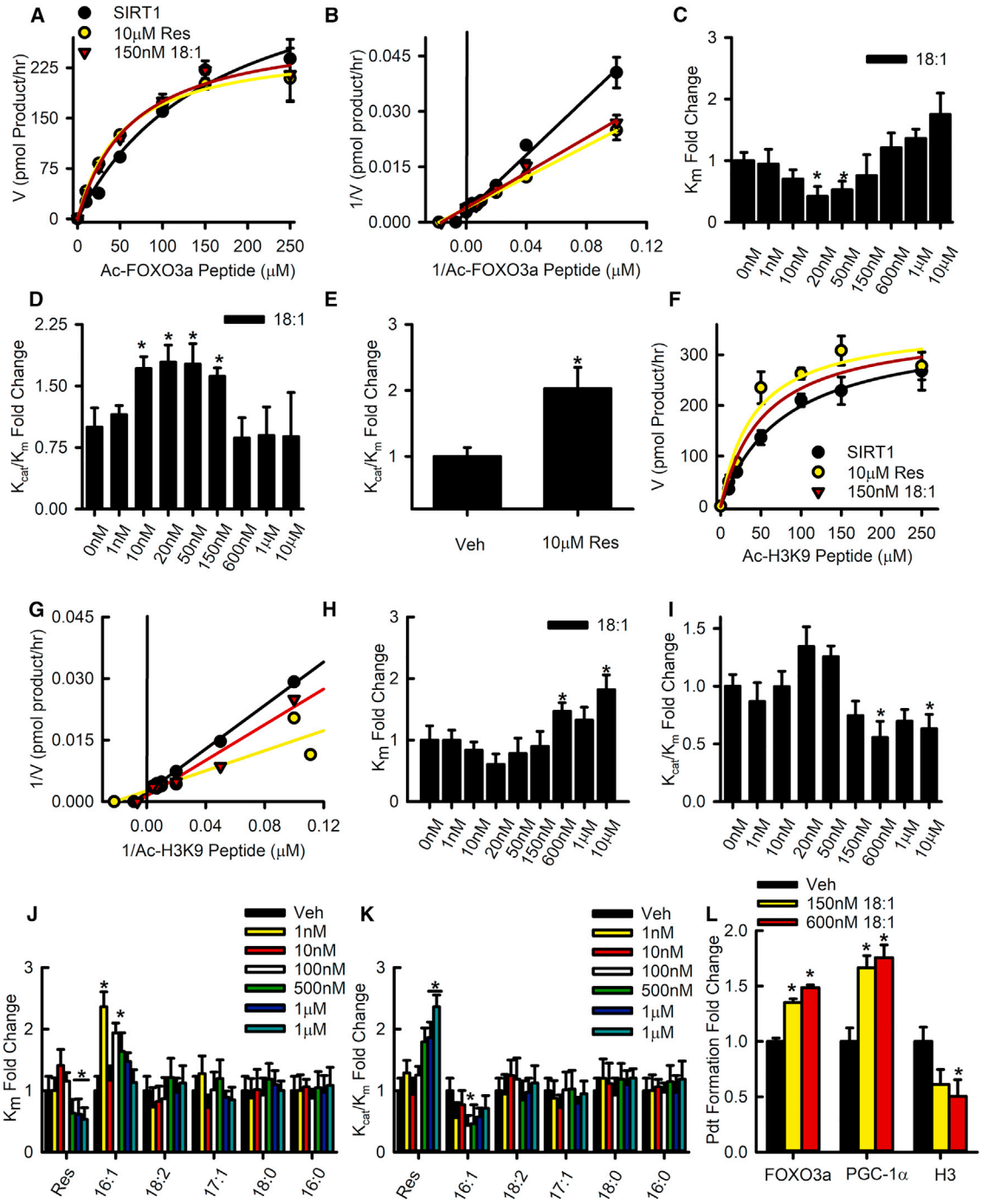

Figure 2. MUFAs Selectively Activate SIRT1

(A) Saturation plot of SIRT1 activity toward FOXO3a and the effects of 18:1 and resveratrol. Data represent the mean ± SEM from quadruplicate experiments.

(B) Lineweaver-Burk reciprocal plots were generated to determine K_m, V_{max}, and K_{cat} for the FOXO3a peptide substrate. Data represent the mean ± SEM from quadruplicate experiments.

(C and D) K_m and K_{cat}/K_m fold change for each concentration of 18:1 on FOXO3a. Data represent the mean ± SEM from quadruplicate experiments. * $p < 0.05$.

(E) K_{cat}/K_m fold change for resveratrol (Res; 10 μM). Data represent the mean ± SEM from quadruplicate experiments. * $p < 0.05$.

(F) Saturation plot of SIRT1 activity toward H3 and the effects of 18:1 and resveratrol. Data represent the mean ± SEM from quadruplicate experiments.

(G) Lineweaver-Burk reciprocal plots for the H3 peptide substrate. Data represent the mean ± SEM from quadruplicate experiments.

(H and I) K_m (H) and K_{cat}/K_m (I) fold change for each concentration of 18:1 with H3. Data represent the mean ± SEM from quadruplicate experiments. * $p < 0.05$.

(legend continued on next page)

As expected, cAMP treatment or *Atgl, Sirt1,* and *Pgc-1α* overexpression individually and synergistically increased PGC-1α activity (Figure 3A). Preloading the hepatocytes with 18:1 further enhanced the response to cAMP and protein overexpression on PGC-1α activity, indicating a synergistic effect of MUFA enrichment in LDs, cAMP, and key proteins involved in LD-nuclear MUFA signaling; no effects of 18:1 were observed with *Plin2* overexpression (Figure 3A). To determine if the lipid loading effect was due to the presences of MUFAs rather than fatty acids in general, the experiments were repeated using individual fatty acids 18:1, 18:0, 16:1, and 16:0 (Figure 3B), or a physiological mixture of the fatty acids that included or lacked 18:1 (Figure 3C; Table S3). The individual fatty acids 18:1 and 16:1 synergized with cAMP to increase PGC-1α activity above non-loaded or 18:0/16:0 loaded cells (Figure 3B). The physiological fatty acid mixture containing 18:1 increased PGC-1α activity above the physiological mixture lacking 18:1 and above cells not loaded with lipid in response to cAMP (Figure 3C), a result similar to that of the individual fatty acids. Inhibition of PKA or ATGL negated the effects of 18:1 and cAMP. Taken together, the individual or physiological mixture of fatty acids experiments indicate the enhancing effect was due to the presences of MUFAs rather than fatty acids in general, as saturated fatty acids or mixtures of polyunsaturated fatty acids lacking 18:1 did not enhance PGC-1α activity. Studies utilizing PKA or ATGL inhibitors revealed that PKA-stimulated lipolysis was required for 18:1 mediated activation of PGC-1α in contrast to more traditional SIRT1 activating compound resveratrol (Figure 3B). This indicates MUFAs must be released from LDs by ATGL for activation to occur. In addition, studies utilizing mouse embryonic fibroblasts (MEFs) lacking *Sirt1* revealed that SIRT1 was required for 18:1 mediated regulation of PGC-1α activity (Figures 3D and 3E). Rescue experiments utilizing a GFP-tagged human *Sirt1* construct restored cAMP, 18:1, and resveratrol activation, while the *Sirt1*-E230K mutant, shown to block resveratrol binding (Dai et al., 2015; Hubbard et al., 2013; Sinclair and Guarente, 2014), restored basal and cAMP stimulated PGC-1α activity but did not restore MUFA or resveratrol mediated regulation of PGC-1α (Figure 3F).

Acute exposure of cells to 18:1 has been shown to increase cellular cAMP as a means to activate SIRT1 (Lim et al., 2013). Therefore, we tested if alterations in cellular cAMP levels contributed to the effects of MUFAs on SIRT1 activation in cells (Figures 3G and 3H). Acute exposure (6 h) to 18:1 increased basal PGC-1α activity while chronic or overnight exposure (16 h) did not. Both acute and overnight 18:1 loading enhanced PGC-1α activity above non-loaded cells upon stimulation of β-andrenergic signaling. Inhibition of ATGL mediated lipolysis via ATGLstatin blocked the effects of β-andrenergic stimulation in 18:1 loaded cells. Cells acutely loaded with 18:1 still had elevated basal PGC-1α activity in the presence of ATGLstatin; however, the stimulated response was blocked. Acute 18:1 exposure increased cellular cAMP levels similar to what was previously reported (Lim et al., 2013); however, non-loaded, acutely loaded, and overnight loaded cells all exhibited similar levels of cellular cAMP upon treatment with isoproterenol/IBMX (Figure 3H). Thus, in the experimental conditions where MUFAs and β-andrenergic stimulation synergize to enhance PGC-1α activity in a SIRT1-dependent manner, cAMP levels were not altered between non-loaded and 18:1 loaded cells. While these results are consistent with our data showing ATGL-mediated activation of PGC-1α synergizes with cAMP/PKA, it should be noted that MUFAs also can signal acutely via regulation of cAMP independent of incorporation into and subsequent hydrolysis from LDs.

Olive Oil Diet Increases Oxidative Metabolism in a SIRT1-Dependent Manner

To investigate the effects of SIRT1 activating MUFAs *in vivo*, mice were fed diets enriched in lard and soybean oil (CTRL) or olive oil (OO), which contains ~75% 18:1 (Table S4), and were fasted overnight prior to sacrifice to stimulate lipolytic signaling. OO feeding decreased body weight over the course of 12 weeks due to a decrease in fat mass (Figures S3A–S3C). Without affecting energy intake or locomotion, OO feeding increased oxygen consumption and heat production, leading to increased energy expenditure (EE; Figures S3D–S3N). To determine if the OO in the diet was exerting its physiological effects in a SIRT1-dependent manner, EX527, a potent and specific SIRT1 inhibitor, was administered over the course of three days prior to sacrifice (Figure S4A). SIRT1 inhibition negated the decrease in body weight (Figure 4A) and the increase in serum β-hydroxybutyrate and free fatty acids observed with OO feeding (Figures 4B and 4C). The OO diet reduced white adipose tissue weights, an effect that was normalized in mice treated with EX527 (Figures S4B–S4G). OO feeding decreased hepatic LD size and liver TAG content while SIRT1 inhibition ablated these effects (Figures 4D–4F). Acetylation of SIRT1 targets PGC-1α and FOXO3a were decreased in OO-fed mice, an effect that was attenuated by EX527 (Figures 4G and 4H). To further test the importance of SIRT1 in MUFA-mediated signaling, we determined gene expression of key PGC-1α/PPARα oxidative genes (Figure S5A). Consumption of the OO diet universally increased the expression of PGC-1α/PPAR-α target genes, but these effects were ablated with EX527. The increased gene expression in OO-fed mice corresponded to increased protein abundance of UCP1, PGC-1α, CPT1α, and various respiratory chain complex proteins in the liver (Figures 4I, 4J, and S5B). In addition to hepatic changes, histological examination of interscapular brown adipose tissue exhibited smaller LDs and decreased TAG (Figures 4K–4M), indicative of enhanced thermogenesis. The smaller LDs corresponded to increased protein abundance of oxidative metabolism genes including UCP1, PLIN5, PGC-1α, CPT1α, and complex I, II, III, and IV of the respiratory chain (Figures 4N, 4O, and S5C). Similarly, OO feeding decreased LD size in inguinal white adipose tissue (Figures S5D and S5E) along with increased protein abundance of UCP1, PGC-1α, CPT1α, and

(J and K) K_m (J) and K_{cat}/K_m (K) fold change for each concentration of resveratrol and fatty acids for the H3 peptide substrate. Data represent the mean ± SEM from quadruplicate experiments. * $p < 0.05$.

(L) Competition assay of SIRT1 activity toward FOXO3a, PGC-1α, and H3 acetylated peptide substrates. Data represent the mean ± SEM from quadruplicate experiments. * $p < 0.05$.

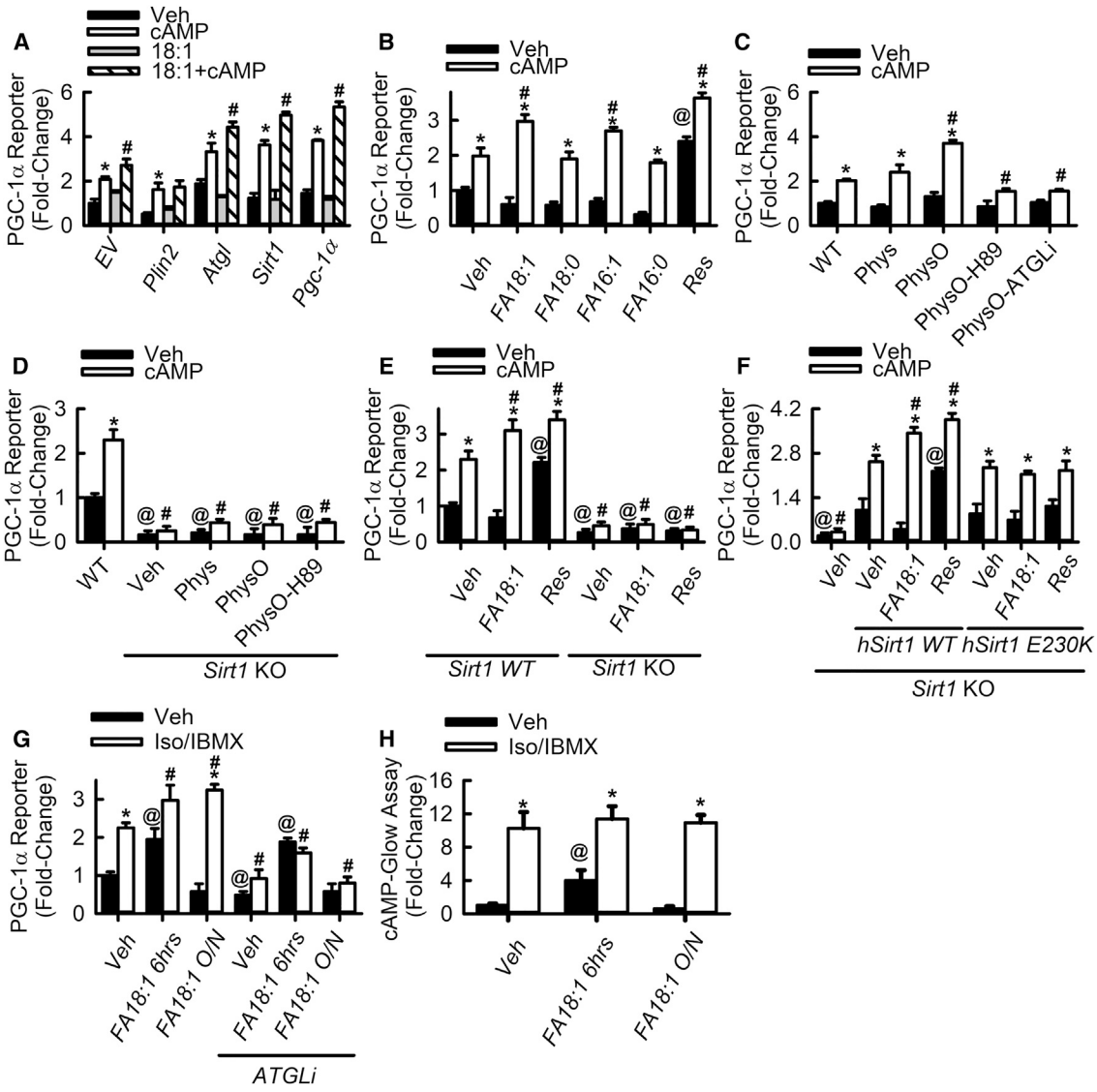

Figure 3. Lipolytically Derived MUFAs Synergize with cAMP and Signal via SIRT1 to Activate PGC-1α

(A) PGC-1α luciferase reporter assays in primary hepatocytes transfected with the various overexpression plasmids (n = 6–12). Data represent the mean ± SEM. *p < 0.05 versus drug veh, #p < 0.05 versus cAMP alone.

(B) PGC-1α luciferase reporter assays in MEFs loaded with saturated fatty acids, MUFAs, or resveratrol (n = 6–12). Data represent the mean ± SEM. *p < 0.05 versus drug veh, #p < 0.05 versus lipid veh treated with cAMP.

(C) PGC-1α luciferase reporter assays in hepatocytes loaded with a physiological mix of fatty acids lacking 18:1 (Phys) or a physiological mix enriched in 18:1 (PhysO). ATGL inhibition was achieved by the addition of 30 μM ATGListatin (ATGLi). PKA inhibition was achieved by addition of 15 μM H89. Both drugs were administered for 1 h followed by addition of 8-bromoadenosine 3′,5′-cyclic monophosphate (cAMP; 1mM). (n = 6–12). Data represent the mean ± SEM. *p < 0.05 versus drug veh, #p < 0.05 versus wild-type cells not loaded with lipid treated with cAMP.

(D) PGC-1α luciferase reporter assays in wild-type or *Sirt1* knockout MEFs preloaded with as physiological mix of fatty acid and subsequently treated with inhibitors (n = 6–12). Data represent the mean ± SEM. *p < 0.05 versus drug veh, @p < 0.05 versus wild-type, #p < 0.05 versus wild-type cells treated with cAMP.

(E) PGC-1α luciferase reporter assays in wild-type or *Sirt1* knockout MEFs exposed to fatty acid or resveratrol preloading (n = 6–12). Data represent the mean ± SEM. *p < 0.05 versus wild-type treated with drug veh, @p < 0.05 versus lipid veh wild-type, #p < 0.05 versus lipid veh wild-type cells treated with cAMP.

(F) PGC-1α reporter assays from *Sirt1* knockout cells transfected with human *Sirt1* or human *Sirt1* E230K mutant (n = 8–12). Data represent the mean ± SEM. *p < 0.05 versus drug veh, @p < 0.05 versus lipid veh-treated *hSirt1*-expressing cells, #p < 0.05 versus lipid veh-treated *hSirt1*-expressing cells treated with cAMP.

(G) PGC-1α reporter assays in MEFs loaded with 500 μM 18:1 acutely (6 h) or overnight (O/N, 16 h). Lipolytic activation was achieved by the addition of 20 μM isoproterenol and 500 μM IBMX. ATGL inhibition was achieved by the addition of 30 μM ATGListatin (ATGLi) (n = 6–12). Data represent the mean ± SEM. *p < 0.05 versus drug veh, @p < 0.05 versus lipid veh, #p < 0.05 versus lipid veh treated with Iso/IBMX.

(H) Cellular cAMP levels were measured in MEF cells loaded acutely overnight with 500 μM 18:1 (n = 12–16). Lipolytic activation was achieved by the addition of 20 μM isoproterenol and 500 μM IBMX. Data represent the mean ± SEM. *p < 0.05 versus drug veh, @p < 0.05 versus lipid veh without Iso/IBMX, #p < 0.05 versus lipid veh treated with Iso/IBMX.

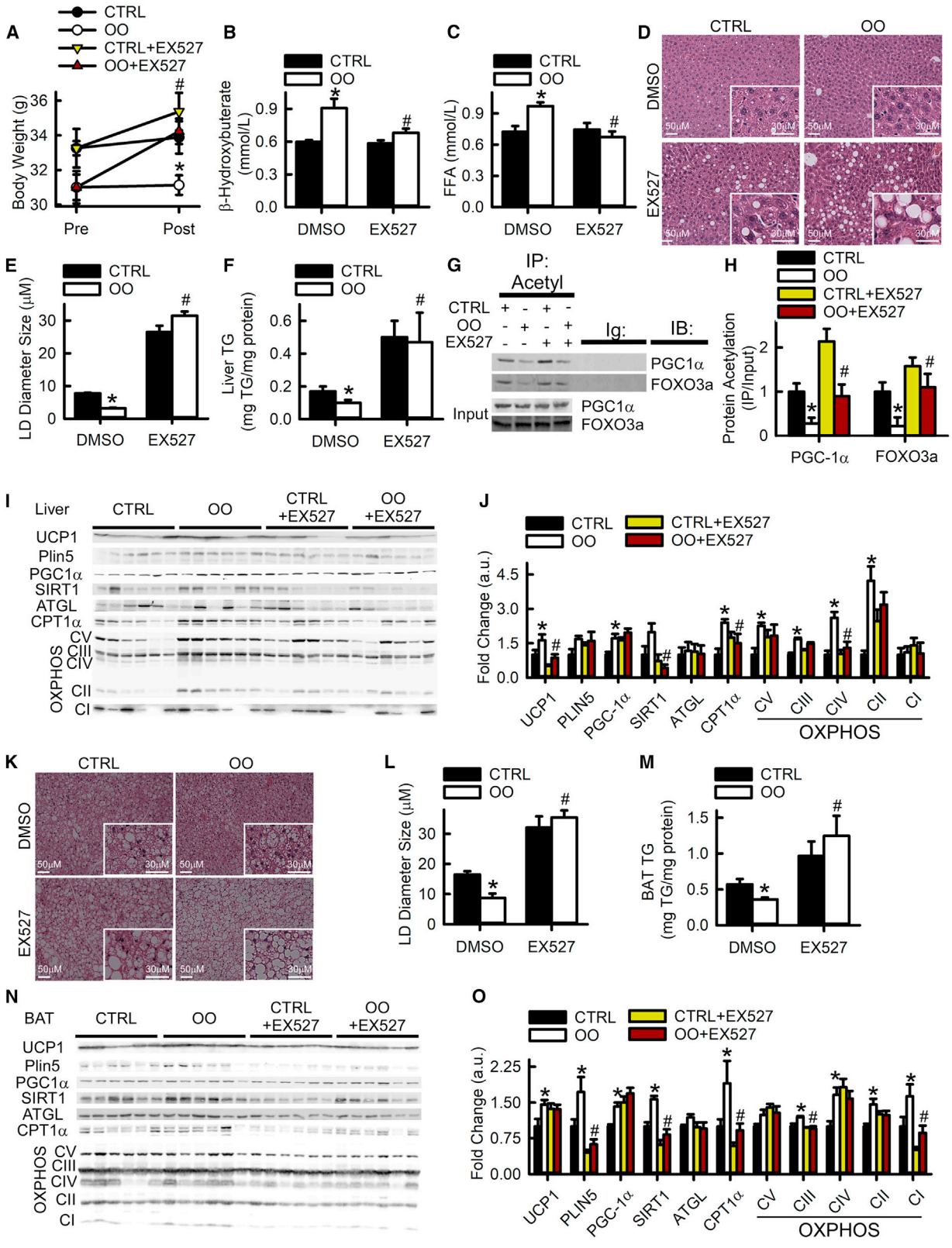

(legend on next page)

respiratory chain complexes I, II, and IV (Figures S5F–S5H). Taken together, these findings define an ATGL-MUFA-SIRT1 axis that is critical for LD signaling to promote PGC-1α/PPAR-α and oxidative metabolism.

ATGL-Mediated Activation of PGC-1α Requires PLIN5

PLIN5 co-localizes and interacts with ATGL, suggesting that these two proteins may have bi- or unidirectional influence over one another (Granneman et al., 2011). Following PKA activation and its phosphorylation, PLIN5 translocates from LDs to the nucleus, where it forms a complex with SIRT1 and PGC-1α to promote mitochondrial biogenesis in brown adipose tissue and muscle (Gallardo-Montejano et al., 2016). Given these links between ATGL, PLIN5, SIRT1, and PGC-1α, we investigated the role of PLIN5 in ATGL-mediated activation of SIRT1/PGC-1α. In hepatocytes, we found that ATGL preferentially colocalized with PLIN5-coated LDs (Figure S6A) and translocated to the nucleus to directly interact with SIRT1/PGC-1α in response to fasting or cAMP signaling (Figures S6B–S6D; Table S5). To test if PLIN5 is required for ATGL-mediated signaling, we used CRISPR/Cas9 to knockout *Plin5* in mouse L-cells or antisense oligonucleotides (ASOs) to knockdown *Plin5* in mouse primary hepatocytes (Figures S6E and S6F). Cell-permeable cAMP (8-bromo-cAMP) and ATGL overexpression both individually and synergistically enhanced PGC-1α transcriptional activity in wild-type cells as expected, but ablation of *Plin5* abrogated these effects (Figures 5A and 5B). Rescuing the expression of PLIN5 in *Plin5* knockout cells restored PGC-1α activity, but this restoration required ATGL lipolytic activity (Figure 5A). Moreover, the increase in PGC-1α activity in response to PLIN5 overexpression and cAMP was blocked by chemical inhibition of ATGL or SIRT1 (Figure 5B). Similarly, adenoviral-mediated ATGL overexpression in the livers of mice increased the expression of PGC-1α/PPAR-α target genes; however, ASO-mediated ablation of *Plin5* negated these effects (Figures 5C and S6F). In response to cAMP, PLIN5 undergoes PKA-mediated phosphorylation at Ser155 (Gallardo-Montejano et al., 2016; Pollak et al., 2015), which was verified with an antibody we generated specifically for this phosphorylation site (Figure S6G). Using PLIN5 phospho-mimetic (pM; S155E) and phospho-dead (pD; S155A) mutants, we confirmed that this phosphorylation is both necessary and sufficient for nuclear translocation (Figure S6H). Consistent with an important role of translocation, expression of the PLIN5-pD in the knockout cells was unable to restore the response to cAMP on PGC-1α activity (Figure 5D). Expression of a PLIN5-pM increased basal PGC-1α transcriptional activity but negated the response to cAMP (Figure 5D). However, the increase in basal PGC-1α activity in the PLIN5-pM expressing cells required ATGL activity, suggesting that ATGL-catalyzed lipolysis is critical for PLIN5-mediated signaling. To determine if PLIN5 translocation is dependent on ATGL-catalyzed lipolysis, we knocked down *Atgl* in mouse primary hepatocytes and liver as described previously (Ong et al., 2011). PLIN5 was still able to translocate to the nucleus in response to cAMP (cells) or overnight fasting (livers) following *Atgl* knockdown (Figures 5E and 5F). Thus, these data show that ATGL and PLIN5 are co-obligatory to increase PGC-1α activity and that ATGL inhibition does not influence PKA-mediated translocation of PLIN5 to the nucleus.

PLIN5 Binds Fatty Acids

The above data suggest that an intrinsic function of PLIN5, independent of translocation, is critical for its signaling properties. Aligning the PLIN5 amino acid sequence to its family members highlights a C-terminal region of PLIN5 that is homologous to PLIN2 and PLIN3 (Figures 6A and S7A). The C-terminal regions of PLIN2 and PLIN3 are α-helical and consist of one α−β domain and a 4-helix bundle that comprise a hydrophobic pocket identified to bind fatty acids (Hickenbottom et al., 2004; Najt et al., 2014). We therefore carried out secondary structure analysis of PLIN5 using several prediction programs. Results from the algorithms predict that an α−β domain and 4-helix bundle found in PLIN2/3 exists in PLIN5 (Figure 6B). We next constructed a homology 3D-model of the structure of C-terminal residues 164–390 of murine PLIN5 (Figure 6C) aligned with murine PLIN3, which shares 42% sequence identity. Based on the structural model, PLIN5 contained a hydrophobic binding pocket of sufficient size and character to bind lipids similar to PLIN2 (Najt et al., 2014).

To determine if PLIN5 binds fatty acids, we employed tryptophan fluorescence assays with recombinant full-length murine PLIN5 (Figure S7B). Saturable binding curves for stearic acid (18:0), oleic acid (18:1), palmitic acid (16:0), palmitoleic acid (16:1), and arachidonic acid (20:4) were observed (Figure 6D). K_d values ranged from of 82 to 254 nM with the highest affinity

Figure 4. MUFAs Increase Oxidative Metabolism *In Vivo* through SIRT1 Activation

(A) Body weight of mice fed a control diet (CTRL) or a diet enriched in olive oil (OO). Three days prior to sacrifice, mice were injected with 10 mg/kg of EX527. Body weights were determined before and after EX527 treatment (n = 6–8). Data represent the mean ± SEM.

(B and C) Serum β-hydroxybutyrate (B) and free fatty acid (C) levels in C57BL/6 mice were fed diets low in MUFAs (CTRL; black bars) or enriched in 18:1 (OO; white bars). A subset of mice was injected with 10 mg/kg daily of the SIRT1 inhibitor EX527 for 3 days prior to sacrifice (n = 6–8). Data represent the mean ± SEM.

(D and E) H&E staining (D) of liver tissues from CTRL and OO-fed mice. LD size (E) was determined using 3–4 images from 2–3 mice per group.

(F) Quantification of TAG in liver samples was determined using 3–4 mice per group. Data represent the mean ± SEM.

(G) western blots of total and acetylated-PGC-1α and FOXO3a in livers from 3–4 mice.

(H) Quantification of immunoprecipitated acetylated-PGC-1α and FOXO3a. Data represent the mean ± SEM from triplicate experiments.

(I and J) Relative protein expression levels of UCP1, PLIN5, PGC-1α, SIRT1, ATGL, CPT1α, and OXPHOS complex CI-V in liver were determined by western blotting (I) (n = 6) and quantified by densitometric analysis (J). Data represent the mean ± SEM.

(K and L) H&E staining (K) of brown adipose tissue (BAT) from CTRL and OO-fed mice. LD size (L) was determined using 3–4 images from 2–3 mice per group.

(M) Quantification of TAG in BAT samples was determined using 3–4 mice per group. Data represent the mean ± SEM.

(N and O) Relative protein expression levels of UCP1, PLIN5, PGC-1α, SIRT1, ATGL, CPT1α, and OXPHOS complex CI-V in BAT were determined by western blotting (N) (n = 6) and quantified by densitometric analysis (O). Data represent the mean ± SEM. *$p < 0.05$ versus CTRL diet, $^{\#}p < 0.05$ versus DMSO.

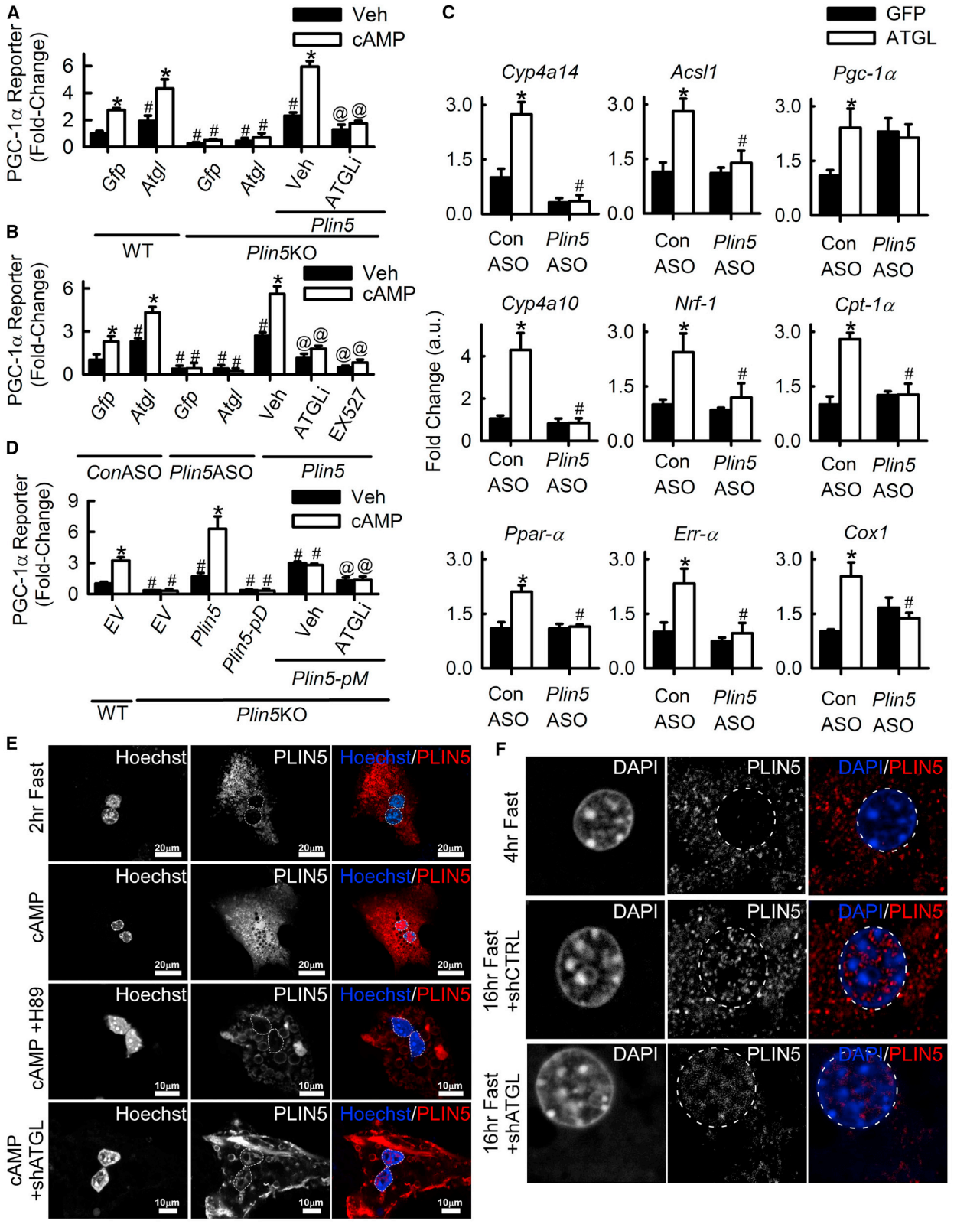

(legend on next page)

determined with the monounsaturated fatty acids (MUFAs) 16:1 (82 ± 12 nM) and 18:1 (89 ± 2 nM). Similar analyses of the PLIN5 phospho mutants with the two MUFAs were performed. PLIN5-pD exhibited a similar K_d to wild-type PLIN5, but the PLIN5-pM exhibited a 3.4- and 2.4-fold increase in binding affinity for 16:1 (23 ± 3 nM versus 79 ± 2 nM) and 18:1 (36 ± 8 nM versus 87 ± 9 nM), respectively (Figure 6E). Fluorescence binding and displacement assays using (1,8,-ANS) as described above were conducted to further verify lipid binding (Kane and Bernlohr, 1996). Displacement of the bound fluorophore with natural ligands resulted in K_i values 4 ± 0.13 μM, 9.9 ± 0.07 μM, 17.7 ± 0.04 μM, and 44.9 ± 0.02 μM for 18:1, 16:1, 18:0, and 22:4, respectively (Figure S7C; Table S6). To examine how phosphorylation affects function, the secondary structures of PLIN5 and the phosphorylation mutants, in the presence or absence of ligands, were analyzed by circular dichroism (CD). In absence of ligand, the CD spectrum for PLIN5-pD was not statistically different from that of PLIN5 (Figure 6F). Analysis of CD spectra revealed that PLIN5-pM exhibited decreased helical content, and increased beta and random coil content over PLIN5-pD and wild type suggested that phosphorylation of PLIN5 causes the protein to undergo large conformational changes (Table S7). The addition of 18:1 robustly altered the shape of the CD spectrum of PLIN5-pM while more subtle changes were observed with the PLIN5-pD. These alterations were reflected by increases in both rigid and disordered helices while decreasing the percentage of β sheets (Figure 6F; Table S7). In summary, the CD results were consistent with the predicted secondary structure and indicated that the proteins were sensitive to fatty acid binding. Phosphorylation of PLIN5 alters the overall structure of the protein shifting from helical to β sheet and β-turn, while addition of a fatty acid changes the overall fold of PLIN5-pM back to a more helical fold.

MUFA Allosteric Regulation of SIRT1/PGC-1α Requires PLIN5

The link between lipolysis to changes in SIRT1/PGC-1α signaling and oxidative gene expression is enhanced in the presences of MUFAs while signaling between LDs and SIRT1/PGC-1α requires PLIN5. We therefore tested the effects of PLIN5 deletion on MUFA activation of SIRT1. Studies utilizing L-cells lacking *Plin5* revealed that PLIN5 was required for 18:1 mediated regulation of PGC-1α activity (Figure S7D). Transfection of the *Plin5*-pD mutant into the *Plin5* knockout cells was unable to restore PGC-1α activity (Figure S7E). Rescuing PLIN5 expression with transfection of the *Plin5*-pM plasmid restored basal PGC-1α activity, but the cells were unable to respond to cAMP and/or 18:1 loading, suggesting that PLIN5 has to be present on the LD surface to acquire the fatty acid prior to nuclear translocation and SIRT1 activation (Figure S7F).

DISCUSSION

Numerous studies have linked lipolysis, mediated through manipulation of ATGL or other LD proteins, to changes in PGC-1α/PPARα signaling and oxidative gene expression (Ahmadian et al., 2009; Haemmerle et al., 2011; Khan et al., 2015; Ong et al., 2011). This signaling is thought to play a key role in increasing the oxidative capacity of the cell to match the supply of lipolytic-supplied fatty acids. PLIN5 has been widely studied as a key LD protein that promotes oxidative metabolism and uncouples LD accumulation from lipotoxicity and insulin resistance (Bosma et al., 2013; Mason et al., 2014; Pollak et al., 2015; Sztalryd and Brasaemle, 2017; Wolins et al., 2006). Our data identify a novel role of PLIN5 in fatty acid binding and transport as an underlying mechanism that couples lipolysis to SIRT1/PGC-1α signaling (Figure 7). In addition, PKA-mediated phosphorylation is a key event that both increases the ability of PLIN5 to bind fatty acids, preferentially MUFAs, and trigger its translocation to the nucleus. These finding also implicate potential interactions between dietary lipids, PLIN5 expression, and dietary or environmental stimuli, such as fasting, caloric restriction, or exercise that increase cAMP/PKA signaling to promote lipolysis. Indeed, PLIN5 expression is induced by fasting, caloric restriction, and exercise (Nogueira et al., 2012; Shepherd et al., 2013; Wolins et al., 2006). Taken together, these data unravel a novel mechanism through which PLIN5 elicits its protective effects against lipotoxicity and couples lipolysis to changes in oxidative metabolism (Figure 7).

SIRT1 has a wide range of biological functions including chromatin structure maintenance, cell cycle control, metabolism, and the regulation of healthspan (Banks et al., 2008; Bordone et al., 2007; Pfluger et al., 2008). Resveratrol and other naturally occurring polyphenols activate SIRT1 in a substrate-dependent manner (Borra et al., 2005; Cao et al., 2015; Feldman et al., 2012) similar to what we observed with the selective activation of SIRT1 toward PGC-1α and FOXO3a, but not H3, in response

Figure 5. ATGL-Mediated Activation of PGC-1α Requires PLIN5

(A) PGC-1α luciferase reporter assays in wild-type or *Plin5* knockout mouse L-cells transduced with control (*Gfp*) or *Atgl* adenoviruses. Rescue experiments were performed with overexpression of a plasmid harboring mCherry-*Plin5*. ATGL inhibition was achieved by the addition of 30 μM ATGListatin (ATGLi) (n = 6). Data represent the mean ± SEM. *p < 0.05 versus veh, $^{\#}$p < 0.05 versus wild-type, $^{@}$p < 0.05 versus within treatment vehicle.

(B) PGC-1α luciferase reporters in primary hepatocytes transfected with control (*Ctrl*) or *Plin5* ASOs. Treatment with EX527 (30 μM) was used to inhibit SIRT1 (n = 6–12). Data represent the mean ± SEM. *p < 0.05 versus veh, $^{\#}$p < 0.05 versus *Ctrl* ASO, $^{@}$p < 0.05 versus within treatment vehicle.

(C) PGC-1α/PPAR α target gene expression in livers of mice treated with control or *Plin5* ASOs and adenoviruses harboring *Gfp* or *Atgl* (n = 6–8). Data represent the mean ± SEM. *p < 0.05 versus GFP, $^{\#}$p < 0.05 versus *Con* ASO.

(D) PGC-1α luciferase reporters in wild-type or *Plin5* knockout mouse L-cells transfected with an empty mCherry-vector (*EV*), mCherry-*Plin5*, mCherry-*Plin5-pD*, or mCherry-*Plin5-pM* (n = 6). Data represent the mean ± SEM. *p < 0.05 versus veh, $^{\#}$p < 0.05 versus wild-type, @ p < 0.05 versus veh. treated *Plin5-pM* cells.

(E) Confocal imaging of mCherry-*Plin5* transfected cells pretreated with vehicle or the PKA inhibitor H89 (15 μM) for 1 h followed by addition of 8-bromoadenosine 3′,5′-cyclic monophosphate (cAMP; 1mM) for an additional hour. Cells were also transduced with control or shRNA adenoviruses (repeated with 3 individual hepatocyte isolations).

(F) Livers from 4 and 16 h fasted mice were harvested and subjected to histological sectioning and immunostaining to detect PLIN5 (n = 3).

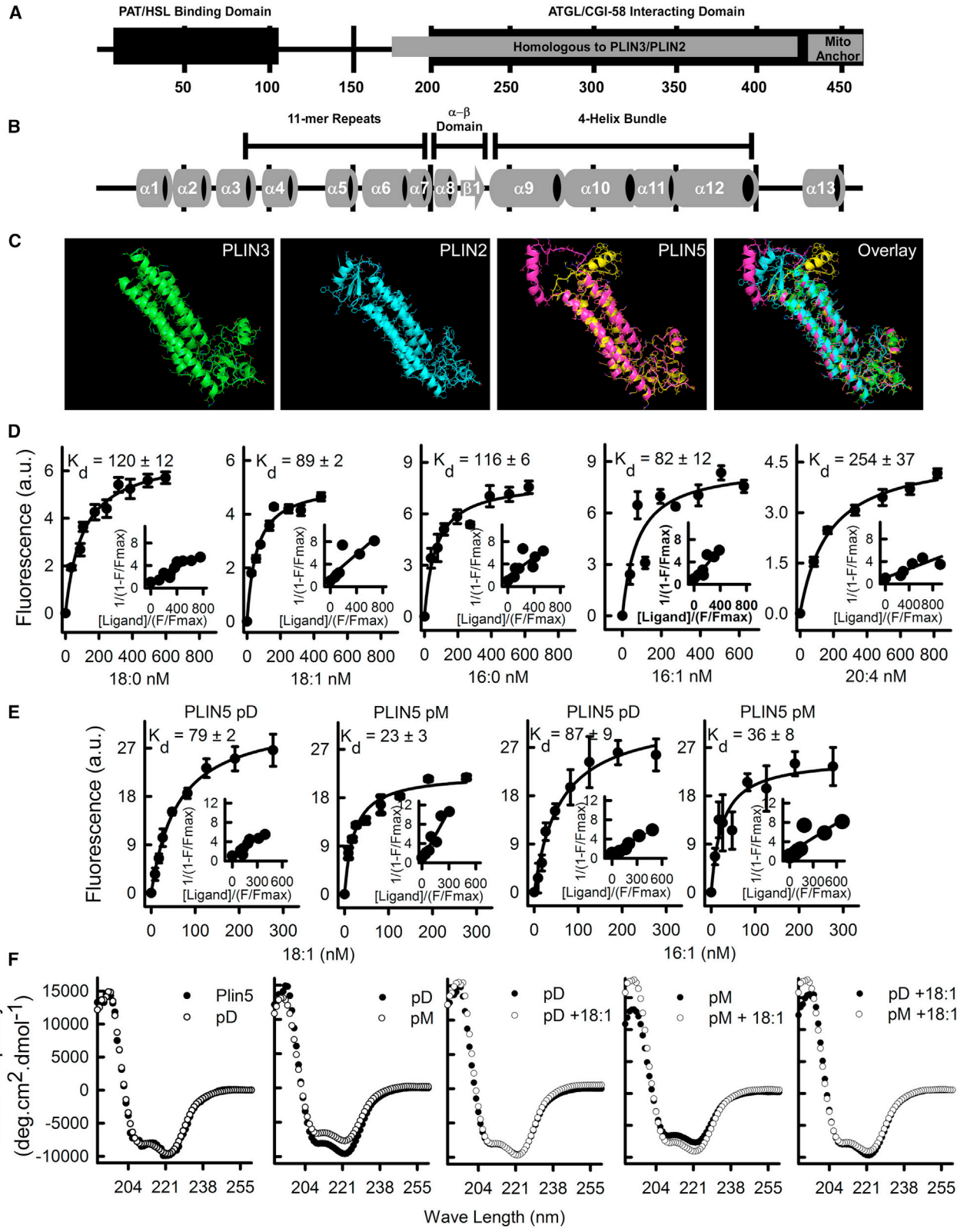

(legend on next page)

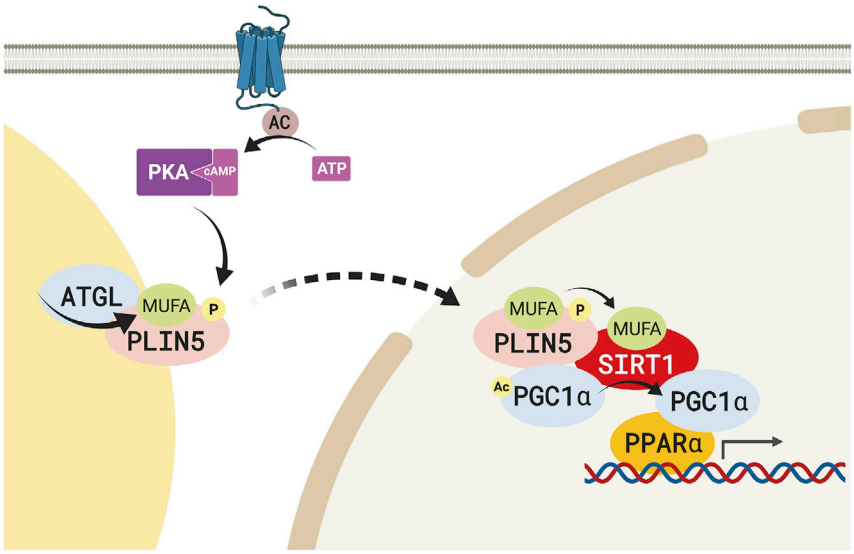

Figure 7. Monounsaturated Fatty Acids Traffic via PLIN5 to Allosterically Activate SIRT1

A model describing lipid droplet derived monounsaturated fatty acids allosterically modulating SIRT1 via PLIN5.

to MUFAs. A previous study has shown that fatty acids do not modulate SIRT1 activity (Feldman et al., 2013). However, this study employed a fixed concentration of 18:1 (100 μM) and used the H3 peptide as a substrate. As we have shown (Figures 1 and 2), MUFAs do not activate SIRT1 at concentrations above 1 μM and do not enhance SIRT1 activity toward the H3 peptide. Our data suggest that in addition to sensing intracellular redox (NAD) and exogenous dietary compounds (e.g., resveratrol), SIRT1 also acts as a nutrient sensor to coordinate LD catabolism with downstream metabolic pathways responsible for the metabolism of fatty acids. The implications of these findings are widespread given the critical role of SIRT1 in many aging-related diseases and lifespan regulation directly linked to nutrient sensing. These studies may also provide a biologically feasible mechanism that underlies the health benefits of MUFAs (Figure 7). MUFAs are common in many foods but are enriched in a variety of foods including nuts, avocados, and olive oil. Evidence from model organism studies through clinical trials bear out the effects of MUFAs and/or olive oil on improvements in oxidative metabolism and energy expenditure (Børsheim et al., 2006; Rodríguez et al., 2002; Shin and Ajuwon, 2018) and in disease prevention and lifespan extension (Buckland and Gonzalez, 2015; Estruch et al., 2006; Han et al., 2017; Salas-Salvadó et al., 2011; Schwingshackl and Hoffmann, 2014a, 2014b; Schwingshackl et al., 2011; Trichopoulou et al., 2005). Importantly, MUFAs are regarded as one of the key components of the Mediterranean Diet, which is well established to have wide-ranging health benefits including reduced aging-related diseases and overall mortality (Sofi et al., 2010). The discovery that resveratrol, which is enriched in red wine, activated SIRT1 was proposed as a mechanism through which a component of the Mediterranean Diet could promote health benefits. However, doses of resveratrol needed to elicit its effects from diet alone far exceeds possible intake (Weiskirchen and Weiskirchen, 2016). While undoubtedly a plethora of components in the Mediterranean Diet contribute to its positive effects on health, the data presented herein provide at least one feasible biological mechanism that may underlie these well-established benefits.

In summary, these studies identify the MUFAs 18:1 and 16:1 as endogenous, non-substrate modulators of SIRT1 that can target the deacetylase to specific protein substrates. Additionally, these findings highlight the importance of LD composition and catabolism as a key regulatory node that integrates physiological inputs (dietary lipids and lipolytic stimuli) to coordinate cellular signaling and metabolism.

Figure 6. PLIN5 Is a Fatty Acid Binding Protein

A) PLIN5 contains several domains of interest including the PAT/HSL binding domain, an ATGL/CGI-58 binding domain, a mitochondria anchor, and a region homologous to PLIN3/PLIN2.

(B) Based on prediction software (SABLE2, SAM, and PsiPRED) and the known X-ray crystal structure of the homologous PLIN3 protein, the predicted secondary structure of PLIN5 contains 13 α helices and 1 small β strand interconnected by random coils and unordered structure.

(C) The X-ray crystal structure of PLIN3 was used to homology model the C-terminal region of PLIN5. The crystal structure of PLIN3 is shown on the farthest left panel (residues 191–437, PDB entry PDB:1SZI). PLIN2 homology model from (Najt et al., 2014) is shown in the second to the left panel, while the PLIN5 models are shown second from the right. Two structures, yellow and pink, were generated by the homology modeler Phyre2 each having a high-probability score. The region that differed between the two PLIN5 models was an α-helix connected to the 4-helix bundle by unordered structure. The structure contains a 4-helix bundle, which together with an α-β domain form the cleft, that when overlaid with the PLIN2 model aligns with the lipid binding pocket outlined in (Najt et al., 2014).

(D) The PLIN5 binding affinity for fatty acids was determined when recombinant protein was titered with increasing amounts of ligand using a quenching of tryptophan fluorescence assay (n = 4). Data represent the mean ± SEM.

(E) PLIN5-pD (S155A) and PLIN5-pM (S155E) binding affinities for MUFAs were determined in a similar manner as PLIN5 (n = 4). Data represent the mean ± SEM.

F) Circular dichroic analysis of PLIN5-pD and PLIN5-pM. Far ultraviolet (UV) circular dichroic (CD) spectra of PLIN5, PLIN5-pD and PLIN5-pM was shown in the presence or absence of ligand. Each spectrum represents an average of ten scans repeated in triplicate. Data represent the mean ± SEM.

STAR★METHODS

Detailed methods are provided in the online version of this paper and include the following:

- KEY RESOURCES TABLE
- LEAD CONTACT AND MATERIALS AVAILABILITY
- EXPERIMENTAL MODEL AND SUBJECT DETAILS
- METHOD DETAILS
  - Mice and adenovirus administration
  - Cell culture
  - PGC-1α reporter assay
  - Site-directed mutagenesis
  - Antisense Oligonucleotides
  - RNA isolation and RT-PCR analysis
  - Live cell and fluorescence resonance energy transfer (FRET) imaging
  - Tissue histology
  - Western blotting
  - Cellular fractionation
  - PLIN5 structural prediction and analysis
  - Expression and purification of recombinant proteins in *Escherichia coli* cells
  - Intrinsic tryptophan fluorescence binding studies
  - Circular-Dichroic analysis of secondary structure
  - 1,8-ANS displacement assays for lipid binding
  - Peptide synthesis and purification
  - HPLC-MS/MS SIRT1 deacetylation assay
  - Dietary experiments
  - Serum analysis
  - Co-immunoprecipitation studies
  - cAMP-Glo Assay
- QUANTIFICATION AND STATISTICAL ANALYSIS
- DATA AND CODE AVAILABILITY

SUPPLEMENTAL INFORMATION

Supplemental Information can be found online at https://doi.org/10.1016/j.molcel.2019.12.003.

ACKNOWLEDGMENTS

We would like to thank Candace Guerrero, Mitchell Fuller, Michael Autry, Colleen Forster, and Guillermo Marques for their technical assistance. We thank the University of Minnesota Imaging Center, Center for Mass Spectrometry and Proteomics, Clinical and Translational Science Biospecimen Support Center, and the Biophysical Technology Center for providing instrumentation and expertise. We thank Eduarado Chini for help with initial SIRT1 assays, Barbara Atshaves for antibodies and protocols, and Ann Hertzel for scientific discussions. Funding was provided for C.P.N. (NIH: T32DK007203 and T32AG029796), T.D.H. (NIH: F32DK109556 and L30DK110338), M.P. (NIH: R01CA182543-S1), M.P.F. (NIH: T32DK083250), D.A.B. (NIH: R01DK053189 and the University of Minnesota E-0917-2), L.S.C. (NIH: R01DK098203), and D.G.M. (NIH: R01AG055452, R01DK108790, R01DK114401, and the American Diabetes Association: 1-16-IBS-203).

AUTHOR CONTRIBUTIONS

D.G.M., C.P.N., T.D.H., L.S.C., and S.A.K. conception and design of research; C.P.N., T.D.H., S.A.K., M.P., J.L.H., L.E.M., M.P.K., K.K.K. and M.T.M. performed experiments; C.P.N., T.D.H., S.A.K., D.G.M. and B.A.W. analyzed data; C.P.N., T.D.H., L.S.C., D.A.B., and D.G.M. interpreted results of experiments; C.P.N., S.A.K., and D.G.M. prepared figures; C.P.N. and D.G.M. drafted manuscript; M.J.G., J.L.H., and L.P. contributed materials and regents necessary for completion of studies; C.P.N., D.G.M., D.A.B., L.S.C., T.D.H., and B.A.W. edited and revised manuscript; C.P.N., S.A.K., T.D.H., B.A.W., M.P., J.L.H, L.E.M., M.P.F., K.K.K., M.J.G., M.T.M., D.A.B., L.P., L.S.C., and D.G.M. approved final version of manuscript.

DECLARATION OF INTERESTS

The authors declare no competing interests.

Received: May 15, 2019
Revised: October 17, 2019
Accepted: December 3, 2019
Published: December 31, 2019

REFERENCES

Ahmadian, M., Duncan, R.E., and Sul, H.S. (2009). The skinny on fat: lipolysis and fatty acid utilization in adipocytes. Trends Endocrinol. Metab. *20*, 424–428.

Aldridge, G.M., Podrebarac, D.M., Greenough, W.T., and Weiler, I.J. (2008). The use of total protein stains as loading controls: an alternative to high-abundance single-protein controls in semi-quantitative immunoblotting. J. Neurosci. Methods *172*, 250–254.

Atshaves, B.P., Petrescu, A.D., Starodub, O., Roths, J.B., Kier, A.B., and Schroeder, F. (1999). Expression and intracellular processing of the 58 kDa sterol carrier protein-2/3-oxoacyl-CoA thiolase in transfected mouse L-cell fibroblasts. J. Lipid Res. *40*, 610–622.

Atshaves, B.P., Storey, S.M., Petrescu, A., Greenberg, C.C., Lyuksyutova, O.I., Smith, R., 3rd, and Schroeder, F. (2002). Expression of fatty acid binding proteins inhibits lipid accumulation and alters toxicity in L cell fibroblasts. Am. J. Physiol. Cell Physiol. *283*, C688–C703.

Balasubramanian, P., Howell, P.R., and Anderson, R.M. (2017). Aging and Caloric Restriction Research: A Biological Perspective With Translational Potential. EBioMedicine *21*, 37–44.

Banks, A.S., Kon, N., Knight, C., Matsumoto, M., Gutiérrez-Juárez, R., Rossetti, L., Gu, W., and Accili, D. (2008). SirT1 gain of function increases energy efficiency and prevents diabetes in mice. Cell Metab. *8*, 333–341.

Bordone, L., Cohen, D., Robinson, A., Motta, M.C., van Veen, E., Czopik, A., Steele, A.D., Crowe, H., Marmor, S., Luo, J., et al. (2007). SIRT1 transgenic mice show phenotypes resembling calorie restriction. Aging Cell *6*, 759–767.

Borra, M.T., Smith, B.C., and Denu, J.M. (2005). Mechanism of human SIRT1 activation by resveratrol. J. Biol. Chem. *280*, 17187–17195.

Børsheim, E., Kien, C.L., and Pearl, W.M. (2006). Differential effects of dietary intake of palmitic acid and oleic acid on oxygen consumption during and after exercise. Metabolism *55*, 1215–1221.

Bosma, M., Sparks, L.M., Hooiveld, G.J., Jorgensen, J.A., Houten, S.M., Schrauwen, P., Kersten, S., and Hesselink, M.K. (2013). Overexpression of PLIN5 in skeletal muscle promotes oxidative gene expression and intramyocellular lipid content without compromising insulin sensitivity. Biochim. Biophys. Acta *1831*, 844–852.

Bu, S.Y., Mashek, M.T., and Mashek, D.G. (2009). Suppression of long chain acyl-CoA synthetase 3 decreases hepatic de novo fatty acid synthesis through decreased transcriptional activity. J. Biol. Chem. *284*, 30474–30483.

Buckland, G., and Gonzalez, C.A. (2015). The role of olive oil in disease prevention: a focus on the recent epidemiological evidence from cohort studies and dietary intervention trials. Br. J. Nutr. *113* (*Suppl 2*), S94–S101.

Cao, D., Wang, M., Qiu, X., Liu, D., Jiang, H., Yang, N., and Xu, R.-M. (2015). Structural basis for allosteric, substrate-dependent stimulation of SIRT1 activity by resveratrol. Genes Dev. *29*, 1316–1325.

Chen, D., Steele, A.D., Lindquist, S., and Guarente, L. (2005). Increase in activity during calorie restriction requires Sirt1. Science *310*, 1641.

Dai, H., Case, A.W., Riera, T.V., Considine, T., Lee, J.E., Hamuro, Y., Zhao, H., Jiang, Y., Sweitzer, S.M., Pietrak, B., et al. (2015). Crystallographic structure of a small molecule SIRT1 activator-enzyme complex. Nat. Commun. *6*, 7645.

Dalen, K.T., Dahl, T., Holter, E., Arntsen, B., Londos, C., Sztalryd, C., and Nebb, H.I. (2007). LSDP5 is a PAT protein specifically expressed in fatty acid oxidizing tissues. Biochim. Biophys. Acta *1771*, 210–227.

Di Sante, G., Wang, L., Wang, C., Jiao, X., Casimiro, M.C., Chen, K., Pestell, T.G., Yaman, I., Di Rocco, A., Sun, X., et al. (2015). Sirt1-deficient mice have hypogonadotropic hypogonadism due to defective GnRH neuronal migration. Mol. Endocrinol. *29*, 200–212.

Estruch, R., Martínez-González, M.Á., Corella, D., Salas-Salvadó, J., Ruiz-Gutiérrez, V., Covas, M.I., Fiol, M., Gómez-Gracia, E., López-Sabater, M.C., Vinyoles, E., et al.; PREDIMED Study Investigators (2006). Effects of a Mediterranean-style diet on cardiovascular risk factors: a randomized trial. Ann. Intern. Med. *145*, 1–11.

Feldman, J.L., Dittenhafer-Reed, K.E., and Denu, J.M. (2012). Sirtuin catalysis and regulation. J. Biol. Chem. *287*, 42419–42427.

Feldman, J.L., Baeza, J., and Denu, J.M. (2013). Activation of the protein deacetylase SIRT6 by long-chain fatty acids and widespread deacylation by mammalian sirtuins. J. Biol. Chem. *288*, 31350–31356.

Finck, B.N., Gropler, M.C., Chen, Z., Leone, T.C., Croce, M.A., Harris, T.E., Lawrence, J.C., Jr., and Kelly, D.P. (2006). Lipin 1 is an inducible amplifier of the hepatic PGC-1α/PPARalpha regulatory pathway. Cell Metab. *4*, 199–210.

Gallardo-Montejano, V.I., Saxena, G., Kusminski, C.M., Yang, C., McAfee, J.L., Hahner, L., Hoch, K., Dubinsky, W., Narkar, V.A., and Bickel, P.E. (2016). Nuclear Perilipin 5 integrates lipid droplet lipolysis with PGC-1α/SIRT1-dependent transcriptional regulation of mitochondrial function. Nat. Commun. *7*, 12723.

Gemmink, A., Bosma, M., Kuijpers, H.J.H., Hoeks, J., Schaart, G., van Zandvoort, M.A.M.J., Schrauwen, P., and Hesselink, M.K.C. (2016). Decoration of intramyocellular lipid droplets with PLIN5 modulates fasting-induced insulin resistance and lipotoxicity in humans. Diabetologia *59*, 1040–1048.

Granneman, J.G., Moore, H.P.H., Krishnamoorthy, R., and Rathod, M. (2009). Perilipin controls lipolysis by regulating the interactions of AB-hydrolase containing 5 (Abhd5) and adipose triglyceride lipase (Atgl). J. Biol. Chem. *284*, 34538–34544.

Granneman, J.G., Moore, H.P., Mottillo, E.P., Zhu, Z., and Zhou, L. (2011). Interactions of perilipin-5 (Plin5) with adipose triglyceride lipase. J. Biol. Chem. *286*, 5126–5135.

Greenberg, A.S., Coleman, R.A., Kraemer, F.B., McManaman, J.L., Obin, M.S., Puri, V., Yan, Q.W., Miyoshi, H., and Mashek, D.G. (2011). The role of lipid droplets in metabolic disease in rodents and humans. J. Clin. Invest. *121*, 2102–2110.

Haemmerle, G., Moustafa, T., Woelkart, G., Büttner, S., Schmidt, A., van de Weijer, T., Hesselink, M., Jaeger, D., Kienesberger, P.C., Zierler, K., et al. (2011). ATGL-mediated fat catabolism regulates cardiac mitochondrial function via PPAR-α and PGC-1. Nat. Med. *17*, 1076–1085.

Hallows, W.C., Lee, S., and Denu, J.M. (2006). Sirtuins deacetylate and activate mammalian acetyl-CoA synthetases. Proc. Natl. Acad. Sci. USA *103*, 10230–10235.

Han, S., Schroeder, E.A., Silva-García, C.G., Hebestreit, K., Mair, W.B., and Brunet, A. (2017). Mono-unsaturated fatty acids link H3K4me3 modifiers to C. elegans lifespan. Nature *544*, 185–190.

Hickenbottom, S.J., Kimmel, A.R., Londos, C., and Hurley, J.H. (2004). Structure of a lipid droplet protein; the PAT family member TIP47. Structure *12*, 1199–1207.

Houtkooper, R.H., Pirinen, E., and Auwerx, J. (2012). Sirtuins as regulators of metabolism and healthspan. Nat. Rev. Mol. Cell Biol. *13*, 225–238.

Hubbard, B.P., and Sinclair, D.A. (2014). Small molecule SIRT1 activators for the treatment of aging and age-related diseases. Trends Pharmacol. Sci. *35*, 146–154.

Hubbard, B.P., Gomes, A.P., Dai, H., Li, J., Case, A.W., Considine, T., Riera, T.V., Lee, J.E., e, S.Y., Lamming, D.W., et al. (2013). Evidence for a common mechanism of SIRT1 regulation by allosteric activators. Science *339*, 1216–1219.

Kaeberlein, M., McDonagh, T., Heltweg, B., Hixon, J., Westman, E.A., Caldwell, S.D., Napper, A., Curtis, R., DiStefano, P.S., Fields, S., et al. (2005). Substrate-specific activation of sirtuins by resveratrol. J. Biol. Chem. *280*, 17038–17045.

Kane, C.D., and Bernlohr, D.A. (1996). A simple assay for intracellular lipid-binding proteins using displacement of 1-anilinonaphthalene 8-sulfonic acid. Anal. Biochem. *233*, 197–204.

Kelley, L.A., and Sternberg, M.J. (2009). Protein structure prediction on the Web: a case study using the Phyre server. Nat. Protoc. *4*, 363–371.

Kelley, L.A., Mezulis, S., Yates, C.M., Wass, M.N., and Sternberg, M.J.E. (2015). The Phyre2 web portal for protein modeling, prediction and analysis. Nat. Protoc. *10*, 845–858.

Khan, S.A., Sathyanarayan, A., Mashek, M.T., Ong, K.T., Wollaston-Hayden, E.E., and Mashek, D.G. (2015). ATGL-catalyzed lipolysis regulates SIRT1 to control PGC-1α/PPAR-α signaling. Diabetes *64*, 418–426.

Kim, D., Nguyen, M.D., Dobbin, M.M., Fischer, A., Sananbenesi, F., Rodgers, J.T., Delalle, I., Baur, J.A., Sui, G., Armour, S.M., et al. (2007). SIRT1 deacetylase protects against neurodegeneration in models for Alzheimer's disease and amyotrophic lateral sclerosis. EMBO J. *26*, 3169–3179.

Kuramoto, K., Okamura, T., Yamaguchi, T., Nakamura, T.Y., Wakabayashi, S., Morinaga, H., Nomura, M., Yanase, T., Otsu, K., Usuda, N., et al. (2012). Perilipin 5, a lipid droplet-binding protein, protects heart from oxidative burden by sequestering fatty acid from excessive oxidation. J. Biol. Chem. *287*, 23852–23863.

Lagouge, M., Argmann, C., Gerhart-Hines, Z., Meziane, H., Lerin, C., Daussin, F., Messadeq, N., Milne, J., Lambert, P., Elliott, P., et al. (2006). Resveratrol improves mitochondrial function and protects against metabolic disease by activating SIRT1 and PGC-1α. Cell *127*, 1109–1122.

Lim, J.-H., Gerhart-Hines, Z., Dominy, J.E., Lee, Y., Kim, S., Tabata, M., Xiang, Y.K., and Puigserver, P. (2013). Oleic acid stimulates complete oxidation of fatty acids through protein kinase A-dependent activation of SIRT1-PGC1α complex. J. Biol. Chem. *288*, 7117–7126.

Mason, R.R., Mokhtar, R., Matzaris, M., Selathurai, A., Kowalski, G.M., Mokbel, N., Meikle, P.J., Bruce, C.R., and Watt, M.J. (2014). PLIN5 deletion remodels intracellular lipid composition and causes insulin resistance in muscle. Mol. Metab. *3*, 652–663.

McIntosh, A.L., Storey, S.M., and Atshaves, B.P. (2010). Intracellular lipid droplets contain dynamic pools of sphingomyelin: ADRP binds phospholipids with high affinity. Lipids *45*, 465–477.

McIntosh, A.L., Senthivinayagam, S., Moon, K.C., Gupta, S., Lwande, J.S., Murphy, C.C., Storey, S.M., and Atshaves, B.P. (2012). Direct interaction of Plin2 with lipids on the surface of lipid droplets: a live cell FRET analysis. Am. J. Physiol. Cell Physiol. *303*, C728–C742.

Miyoshi, H., Perfield, J.W., 2nd, Souza, S.C., Shen, W.J., Zhang, H.H., Stancheva, Z.S., Kraemer, F.B., Obin, M.S., and Greenberg, A.S. (2007). Control of adipose triglyceride lipase action by serine 517 of perilipin A globally regulates protein kinase A-stimulated lipolysis in adipocytes. J. Biol. Chem. *282*, 996–1002.

Miyoshi, H., Perfield, J.W., 2nd, Obin, M.S., and Greenberg, A.S. (2008). Adipose triglyceride lipase regulates basal lipolysis and lipid droplet size in adipocytes. J. Cell. Biochem. *105*, 1430–1436.

Mohktar, R.A.M., Montgomery, M.K., Murphy, R.M., and Watt, M.J. (2016). Perilipin 5 is dispensable for normal substrate metabolism and in the adaptation of skeletal muscle to exercise training. Am. J. Physiol. Endocrinol. Metab. *311*, E128–E137.

Muratore, K.A., Najt, C.P., Livezey, N.M., Marti, J., Mashek, D.G., and Arriaga, E.A. (2018). Sizing lipid droplets from adult and geriatric mouse liver tissue via nanoparticle tracking analysis. Anal. Bioanal. Chem. *410*, 3629–3638.

Najt, C.P., Lwande, J.S., McIntosh, A.L., Senthivinayagam, S., Gupta, S., Kuhn, L.A., and Atshaves, B.P. (2014). Structural and functional assessment of perilipin 2 lipid binding domain(s). Biochemistry *53*, 7051–7066.

Najt, C.P., Senthivinayagam, S., Aljazi, M.B., Fader, K.A., Olenic, S.D., Brock, J.R., Lydic, T.A., Jones, A.D., and Atshaves, B.P. (2016). Liver-specific loss of Perilipin 2 alleviates diet-induced hepatic steatosis, inflammation, and fibrosis. Am. J. Physiol. Gastrointest. Liver Physiol. *310*, G726–G738.

Nogueira, L.M., Lavigne, J.A., Chandramouli, G.V.R., Lui, H., Barrett, J.C., and Hursting, S.D. (2012). Dose-dependent effects of calorie restriction on gene expression, metabolism, and tumor progression are partially mediated by insulin-like growth factor-1. Cancer Med. *1*, 275–288.

Ong, K.T., Mashek, M.T., Bu, S.Y., Greenberg, A.S., and Mashek, D.G. (2011). Adipose triglyceride lipase is a major hepatic lipase that regulates triacylglycerol turnover and fatty acid signaling and partitioning. Hepatology *53*, 116–126.

Ong, K.T., Mashek, M.T., Davidson, N.O., and Mashek, D.G. (2014). Hepatic ATGL mediates PPAR-α signaling and fatty acid channeling through an L-FABP independent mechanism. J. Lipid Res. *55*, 808–815.

Peng, L., Yuan, Z., Ling, H., Fukasawa, K., Robertson, K., Olashaw, N., Koomen, J., Chen, J., Lane, W.S., and Seto, E. (2011). SIRT1 deacetylates the DNA methyltransferase 1 (DNMT1) protein and alters its activities. Mol. Cell. Biol. *31*, 4720–4734.

Perez, M., Blankenhorn, J., Murray, K.J., and Parker, L.L. (2019). High-throughput identification of FLT3 wild-type and mutant kinase substrate preferences and application to design of sensitive in vitro kinase assay substrates. Mol. Cell. Proteomics *18*, 477–489.

Pfluger, P.T., Herranz, D., Velasco-Miguel, S., Serrano, M., and Tschöp, M.H. (2008). Sirt1 protects against high-fat diet-induced metabolic damage. Proc. Natl. Acad. Sci. USA *105*, 9793–9798.

Pollak, N.M., Jaeger, D., Kolleritsch, S., Zimmermann, R., Zechner, R., Lass, A., and Haemmerle, G. (2015). The interplay of protein kinase A and perilipin 5 regulates cardiac lipolysis. J. Biol. Chem. *290*, 1295–1306.

Puigserver, P., Wu, Z., Park, C.W., Graves, R., Wright, M., and Spiegelman, B.M. (1998). A cold-inducible coactivator of nuclear receptors linked to adaptive thermogenesis. Cell *92*, 829–839.

Rodríguez, V.M., Portillo, M.P., Picó, C., Macarulla, M.T., and Palou, A. (2002). Olive oil feeding up-regulates uncoupling protein genes in rat brown adipose tissue and skeletal muscle. Am. J. Clin. Nutr. *75*, 213–220.

Salas-Salvadó, J., Bulló, M., Babio, N., Martínez-González, M.Á., Ibarrola-Jurado, N., Basora, J., Estruch, R., Covas, M.I., Corella, D., Arós, F., et al.; PREDIMED Study Investigators (2011). Reduction in the incidence of type 2 diabetes with the Mediterranean diet: results of the PREDIMED-Reus nutrition intervention randomized trial. Diabetes Care *34*, 14–19.

Sathyanarayan, A., Mashek, M.T., and Mashek, D.G. (2017). ATGL Promotes Autophagy/Lipophagy via SIRT1 to Control Hepatic Lipid Droplet Catabolism. Cell Rep. *19*, 1–9.

Schwingshackl, L., and Hoffmann, G. (2014a). Mediterranean dietary pattern, inflammation and endothelial function: a systematic review and meta-analysis of intervention trials. Nutr. Metab. Cardiovasc. Dis. *24*, 929–939.

Schwingshackl, L., and Hoffmann, G. (2014b). Monounsaturated fatty acids, olive oil and health status: a systematic review and meta-analysis of cohort studies. Lipids Health Dis. *13*, 154.

Schwingshackl, L., Strasser, B., and Hoffmann, G. (2011). Effects of monounsaturated fatty acids on glycaemic control in patients with abnormal glucose metabolism: a systematic review and meta-analysis. Ann. Nutr. Metab. *58*, 290–296.

Senthivinayagam, S., McIntosh, A.L., Moon, K.C., and Atshaves, B.P. (2013). Plin2 inhibits cellular glucose uptake through interactions with SNAP23, a SNARE complex protein. PLoS ONE *8*, e73696, https://doi.org/10.71371/journal.pone.0073696.

Shepherd, S.O., Cocks, M., Tipton, K.D., Ranasinghe, A.M., Barker, T.A., Burniston, J.G., Wagenmakers, A.J.M., and Shaw, C.S. (2013). Sprint interval and traditional endurance training increase net intramuscular triglyceride breakdown and expression of perilipin 2 and 5. J. Physiol. *591*, 657–675.

Shin, S., and Ajuwon, K.M. (2018). Effects of Diets Differing in Composition of 18-C Fatty Acids on Adipose Tissue Thermogenic Gene Expression in Mice Fed High-Fat Diets. Nutrients *10*, E256.

Sinclair, D.A., and Guarente, L. (2014). Small-molecule allosteric activators of sirtuins. Annu. Rev. Pharmacol. Toxicol. *54*, 363–380.

Sofi, F., Abbate, R., Gensini, G.F., and Casini, A. (2010). Accruing evidence on benefits of adherence to the Mediterranean diet on health: an updated systematic review and meta-analysis. Am. J. Clin. Nutr. *92*, 1189–1196.

Sreerama, N., and Woody, R.W. (2000). Estimation of protein secondary structure from circular dichroism spectra: comparison of CONTIN, SELCON, and CDSSTR methods with an expanded reference set. Anal. Biochem. *287*, 252–260.

Storey, S.M., McIntosh, A.L., Huang, H., Landrock, K.K., Martin, G.G., Landrock, D., Payne, H.R., Atshaves, B.P., Kier, A.B., and Schroeder, F. (2012). Intracellular cholesterol-binding proteins enhance HDL-mediated cholesterol uptake in cultured primary mouse hepatocytes. Am. J. Physiol. Gastrointest. Liver Physiol. *302*, G824–G839.

Sztalryd, C., and Brasaemle, D.L. (2017). The perilipin family of lipid droplet proteins: Gatekeepers of intracellular lipolysis. Biochim Biophys Acta Mol Cell Biol Lipids *1862* (10 Pt B), 1221–1232.

Trichopoulou, A., Orfanos, P., Norat, T., Bueno-de-Mesquita, B., Ocké, M.C., Peeters, P.H., van der Schouw, Y.T., Boeing, H., Hoffmann, K., Boffetta, P., et al. (2005). Modified Mediterranean diet and survival: EPIC-elderly prospective cohort study. BMJ *330*, 991.

Wang, C., Zhao, Y., Gao, X., Li, L., Yuan, Y., Liu, F., Zhang, L., Wu, J., Hu, P., Zhang, X., et al. (2015). Perilipin 5 improves hepatic lipotoxicity by inhibiting lipolysis. Hepatology *61*, 870–882.

Weiskirchen, S., and Weiskirchen, R. (2016). Resveratrol: How Much Wine Do You Have to Drink to Stay Healthy? Adv. Nutr. *7*, 706–718.

Willenborg, M., Schmidt, C.K., Braun, P., Landgrebe, J., von Figura, K., Saftig, P., and Eskelinen, E.-L. (2005). Mannose 6-phosphate receptors, Niemann-Pick C2 protein, and lysosomal cholesterol accumulation. J. Lipid Res. *46*, 2559–2569.

Wolins, N.E., Quaynor, B.K., Skinner, J.R., Tzekov, A., Croce, M.A., Gropler, M.C., Varma, V., Yao-Borengasser, A., Rasouli, N., Kern, P.A., et al. (2006). OXPAT/PAT-1 is a PPAR-induced lipid droplet protein that promotes fatty acid utilization. Diabetes *55*, 3418–3428.

STAR★METHODS

KEY RESOURCES TABLE

REAGENT or RESOURCE	SOURCE	IDENTIFIER
Antibodies		
Guinea pig polyclonal anti-PLIN5	Progen	Cat No. GP31
Rabbit polyclonal anti-PLIN2	(McIntosh et al., 2012)	N/A
Rabbit polyclonal anti-ATGL	Cell Signaling Technology	Cat No. 2138S
Rabbit polyclonal anti-FOXO3a	ThermoFisher Scientific	Cat No. PA5-27145; RRID: AB_2544621
Mouse monoclonal anti-PGC-1α	EMD Millipore	Cat No. ST1202; RRID: AB_2237237
Rabbit polyclonal anti-PGC-1α	Abcam	Cat No. ab54481; RRID: AB_881987
Mouse monoclonal anti-Histone H3	Cell Signaling Technology	Cat No. 14269; RRID: AB_2756816
Rabbit monoclonal anti-β Actin	LI-COR	Cat No. 926-42210
Mouse Monoclonal anti-AcLysine	Novis Biologicals	Cat No. 15G10
Mouse Monoclonal anti-AcLysine	Santa Cruz Biotechnology	Cat No. AKL5C1
Mouse Monoclonal anti-AcLysine	Cell Signaling Technology	Cat No. 9681S; RRID: AB_331799
Mouse Monoclonal anti-AcLysine	Thermo Scientific	Cat No. 1C6; RRID: AB_2537177
Rabbit Polyclonal anti-Phos-PLIN5; CLARRGRRW(pS)VELK	NeoBioLab; This Paper	N/A
Rabbit Polyclonal anti-Total-PLIN5; CLARRGRRWSVELK	NeoBioLab; This Paper	N/A
Donkey anti-Guinea pig IRDye 800CW	LI-COR	Cat No. 926-32411
Donkey anti-Guinea pig IRDye 680RD	LI-COR	Cat No. 926-68030
Donkey anti-Rabbit pig IRDye 800CW	LI-COR	Cat No. 926-32213
Donkey anti-Rabbit pig IRDye 680RD	LI-COR	Cat No. 926-68022
Donkey anti-Mouse pig IRDye 800CW	LI-COR	Cat No. 925-32212
Donkey anti-Mouse pig IRDye 680RD	LI-COR	Cat No. 926-68023
Bacterial and Virus Strains		
BL21 (DE3)	New England BioLab	Cat No. C2527H
BL21 (DE3) Codon$^+$	Fisher Scientific	Cat No. NC9122855
XL1-Blue	Agilent	Cat No. 200150
Ad-ATGL	(Miyoshi et al., 2008; Miyoshi et al., 2007)	N/A
Ad-shATGL	(Miyoshi et al., 2008; Miyoshi et al., 2007)	N/A
Chemicals, Peptides, and Recombinant Proteins		
8-bromoadenosine 39,59-cyclic monophosphate	Santa Cruz Biotechnology	Cat No. SC-217493A
Isoproterenol	Sigma-Aldrich	Cat No. I6504
3-isobutyl1-methylxanthine (IBMX)	Sigma-Aldrich	Cat No. I5879
1-anilinonaphthalene 8-sulfonic acid	Molecular Probes	Cat No. A47
M199 media	Sigma-Aldrich	Cat No. M5017
ATGL Statin (ATGLi)	Cayman Chemical	Cat No. 15284
EX527	Cayman Chemical	Cat No. 10009798
H89	Cayman Chemical	Cat No. 10010556
Dynabeads Protein G	ThermoFisher Scientific	Cat No. 10004D
NucBlue	ThermoFisher Scientific	Cat No. R37605
PGC-1α Peptide; KNSWSNETKVIAPNT	This Paper	N/A
Acetyl-PGC-1α; KNSWSNETK(Ac)VIAPNT	This Paper	N/A
Histone H3 Peptide; KWWGGTSKRATQK	This Paper	N/A

(*Continued on next page*)

Continued

REAGENT or RESOURCE	SOURCE	IDENTIFIER
Acetyl-Histone H3; KWWGGTSK(Ac) RATQK	This Paper	N/A
FOXO3a Peptide; KDSPSQLSKWPGSPTS	This Paper	N/A
Acetyl-FOXO3a; KDSPSQLSK(Ac) WPGSPTS	This Paper	N/A
P53 Peptide; WEEKGQSTSSHSK STEGAEE	This Paper	N/A
Acetyl-P53; WEEKGQSTSSHSK(Ac) STEGAEE	This Paper	N/A
P53-W Peptide; WEEKGQSTSSHSKS TEGWEE	This Paper	N/A
Acetyl-P53-W Peptide; WEEKGQSTS SHSK(Ac)STEGWEE	This Paper	N/A
SIRT1	(Hallows et al., 2006)	N/A
PLIN5	This Paper	N/A
Critical Commercial Assays		
Dual-Luciferase Reporter Assay System	Promega	Cat No. E1960
cAMP-Glo Assay	Promega	Cat No. V1501
QuickChange Lightning Site-Directed Mutagenesis Kit	Agilent	Cat No. 210515
Nuclear Complex Co-IP system	Active Motif	Cat No. 54001
β-hydroxybutyrate LiquiColor kit	EKF Diagnostics	Cat No. 2440-058
NEFA-Wako Chemicals lipid assay systems	Wako Chemicals	Cat No. 999-34691, 995-34791, 991-34891, 993-35191
Targetfect Hepatocyte reagent	Targeting Systems	Cat No. Hep-01
Lipofectamine 3000	ThermoFisher Scientific	Cat No. L3000008
Effectene	QIAGEN	Cat No. 301425
SuperScript® VILO™ cDNA Synthesis Kit	Invitrogen	Cat No. 11754-250
Deposited Data		
N/A	N/A	N/A
Experimental Models: Cell Lines		
Mouse Primary Hepatocytes	(Ong et al., 2011)	N/A
Mouse Embryonic Fibroblasts (MEF)	ATCC	Cat No. SCRC-1008
SIRT1 KO Mouse Embryonic Fibroblasts (SIRT1 −/− MEF)	(Di Sante et al., 2015)	N/A
Hep3B	ATCC	Cat No. HB-8064; RRID: CVCL_0326
HepG2	ATCC	Cat No. HB-8065
L-Cells	(Atshaves et al., 2002; McIntosh et al., 2012)	N/A
Perilipin5 KO L-Cells (PLIN5 −/− L-Cells)	This Paper	N/A
Experimental Models: Organisms/Strains		
Male C57BL/6 mice	Envigo	N/A
Oligonucleotides		
Control Anti-Sense Oligonucleotide	Ionis Parmaceuticals; Mark Graham	N/A
Perilipin5 Anti-Sense Oligonucleotide	Ionis Parmaceuticals; Mark Graham	N/A
Recombinant DNA		
pEZ-M98-eGFP-SIRT1	GeneCopoeia	Cat. No EX-Mm12441-M98
pEGFP-hSIRT1	(Peng et al., 2011)	N/A
pEGFP-hSIRT1E230K	This Paper	N/A
pEZ-M98-eGFP-PGC-1α	This Paper	N/A

(*Continued on next page*)

Continued

REAGENT or RESOURCE	SOURCE	IDENTIFIER
pEZ-M55-mCherry-PLIN5	GeneCopoeia	Cat No. EX-Mm27089-M55
pEZ-M55-mCherry-PLIN5-pD (S155A)	This Paper	N/A
pEZ-M55-mCherry-PLIN5-pM (S155E)	This Paper	N/A
pECFP-PLIN2	(McIntosh et al., 2012; Senthivinayagam et al., 2013)	N/A
TK-MH-UASluc	(Finck et al., 2006; Puigserver et al., 1998)	N/A
pRLSV40	(Finck et al., 2006; Puigserver et al., 1998)	N/A
pCMX-GAL4-PGC-1α	(Finck et al., 2006; Puigserver et al., 1998)	N/A
Software and Algorithms		
SigmaPlot 11	Systat Software, Inc	N/A
Prism8	GraphPad	N/A
Canvas 11	Canvas	N/A
PyMOL	PyMOL by Schrodinger	N/A
Image Studio v5	LI-COR Biosciences	N/A
NIS-Elements 4	Nikon	N/A
ZEN	Zeiss	N/A
Cary Eclipse Software	Agilent	N/A
CDSSTR	CDPro	N/A
MultiQuant	Sciex	N/A
Phyre^2	(Kelley et al., 2015; Kelley and Sternberg, 2009)	N/A
MetaMorph 7.5	Molecular Devices	N/A
Other		
Control Diet; 15% Fat Derived from Soybean Oil	Envigo: Teklad Custom Diet	Diet No. TD.170820
Olive Oil Diet; 15% Fat Derived from Olive Oil	Envigo: Teklad Custom Diet	Diet No. TD.170821

LEAD CONTACT AND MATERIALS AVAILABILITY

The lead contact for this study is Douglas Mashek (dmashek@umn.edu). All unique/stable reagents generated in this study are available from the Lead Contact with a completed Materials Transfer Agreement.

EXPERIMENTAL MODEL AND SUBJECT DETAILS

All animal protocols were approved by the University of Minnesota Institutional Animal Care and Use Committee. All cell lines used in this study were cultured in an atmosphere of 37°C, 5% CO_2, 95% humidity. The cell lines are outlined in the legends and STAR Methods table.

METHOD DETAILS

Mice and adenovirus administration

Male 6-8 week old C57BL/6 mice were obtained from Harlan Laboratories and housed under controlled temperature and lighting (20-22°C; 14:10-h light-dark cycle). The mice were fed a purified control diet (TD 94045; Harlan Teklad Premier Laboratory) and acclimatized for 1 week before any experimental procedure.

Cell culture

Primary hepatocytes were isolated as described previously (Bu et al., 2009). Primary hepatocytes were cultured at 37°C under 5% CO_2 in M199 media containing 23 mM HEPES, 26 mM sodium bicarbonate, 10% FBS, 50 IU/mL penicillin, 50 μg/mL streptomycin, 100 nM dexamethasone, 100 nM insulin, and 11 mM glucose and 1 mM carnitine. One hour before treatment with 1 mM of the cAMP analog 8-bromoadenosine 3′,5′-cyclic monophosphate, cells were washed twice with PBS, then allowed to incubate in the same

M199 media minus serum and insulin with the addition of the lipase inhibitor ATGListatin (ATGLi; 30 μM), the cAMP-dependent protein kinase a (PKA) inhibitor H89 (15 μM), or the SIRT1 inhibitor EX527 (30 μM). *Sirt1* knockout mouse embryonic fibroblasts (MEFs) were provided by Michael McBurney (University of Ottawa). *Sirt1* knockout cells were cultured in DMEM supplemented with 10% FBS, 50 IU/mL penicillin, 50 μg/mL streptomycin. Prior to cAMP treatment, cells were cultured in DMEM without FBS. *Plin5* CRISPR/Cas9 knockout L-cells were generated by the University of Minnesota Genome Engineering Shared Resource Center and validated in house (Figure S1G). *Plin5* knockout cells were cultured in DMEM supplemented with 10% FBS, 50 IU/mL penicillin, 50 μg/mL streptomycin. Prior to cAMP treatment, cells were cultured in DMEM without FBS. Adenoviruses to manipulate ATGL expression were generated and used as previously described (Khan et al., 2015; Ong et al., 2014; Sathyanarayan et al., 2017). For single adenovirus treatments, hepatocytes were treated with adenovirus 24-48 hr prior to experimental set-up (Ad-*Atgl* or Ad-*Gfp* and control or *Atgl* shRNA adenoviruses).

PGC-1α reporter assay

Several cell lines were utilized for reporter assays including MEFs, L-cells, primary mouse hepatocytes, *Sirt1* knockout MEFs, and *Plin5* knockout L-cells. In all the reporter experiments cells were transfected with firefly luciferase reporter plasmids (TK-MH-UASluc), control Renilla luciferase (pRLSV40), and GAL4-*Pgc-1a* (pCMX-*GAL4-Pgc*-1*a*) using Targetfect Hepatocyte reagent (Targeting Systems) or Lipofectamine 3000 (ThermoFisher, Grand Island, NY). For overexpression or rescue experiments the following plasmids were co-transfected into cells; CFP-*Plin2* (McIntosh et al., 2012) (Barbara Atshaves, Michigan State University), mCherry-*Plin5* (GeneCopoeia, Rockville MD), eGFP-*Atgl*, eGFP-*Sirt1*, eGFP-*Pgc-1α*, mCherry-*Plin*5 (S155A; pD), mCherry-*Plin*5 (S155D; pM). Cells were stimulated with 1 mM cAMP analog for 6-8 hr. Following treatments with indicated drugs, luciferase activity was measured using the Dual-Luciferase Reporter Assay System (Promega, Fitchburg, WI). Firefly luciferase activity was normalized to the co-expressed Renilla luciferase activity.

Site-directed mutagenesis

To generate mCherry-*Plin*5 S155A, S155E, S155D mutants, QuickChange Lightning Site-Directed Mutagenesis Kit (Agilent; Santa Clara, CA) was used in accordance with the manufacturer's protocol.

Antisense Oligonucleotides

Plin5 and control anti-sense oligonucleotides (ASO) were obtained from Ionis Pharmaceuticals (Carlsbad, CA). The ASO were both used at 40 mg/kg, prepared in sterile saline, and delivered via intraperitoneal injection twice a week for 3 weeks. Knockdown was confirmed through mRNA (RT-PCR) and protein (Western blot) analysis. For use in primary mouse hepatocytes, ASOs were complexed with Effectene transfection reagent (QIAGEN; Venlo, Netherlands) following the manufacturer's protocol.

RNA isolation and RT-PCR analysis

RNA was extracted with Trizol from liver tissues followed by reverse-transcription with SuperScript® VILO cDNA Synthesis Kit (Invitrogen) to generate cDNA. Gene expression was quantified as described previously (Khan et al., 2015; Najt et al., 2016; Ong et al., 2014).

Live cell and fluorescence resonance energy transfer (FRET) imaging

Fluorescence imaging and FRET experiments were performed with cells seeded at a density of 50,000 cells/plate on Mat-Tek cover-glass plates (Ashland, MA). The plasmid expressing mCherry-*Plin5,* eGFP-*Pgc-1α*, and eGFP-*Sirt1* were purchased from GeneCopeia (Rockville, MD) and transfected into mouse primary hepatocytes using Targeting Systems (El Cajon, CA) Targefect Hepatocyte reagent. Digital images were acquired using a Nikon A1Rsi Laser Scanning Confocal Imaging System (LSCIS; Nikon, Melville, NY) equipped with 405 nm, 488 nm, 561 nm, and 640 nm laser, four channel GaSP detectors, and a 60x water immersion objective. To determine subcellular localization of PLIN5 under basal and stimulated conditions, mCherry-*Plin5* overexpressing and control cells were cultured on glass bottom dishes using M199 media containing 23 mM HEPES, 26 mM sodium bicarbonate, 10% FBS, 50 IU/mL penicillin, 50 μg/mL streptomycin, 100 nM dexamethasone, 100 nM insulin, 11 mM glucose, 1 mM carnitine and Hoechst 33342 nuclear dye for 20 min. Cells were washed twice with PBS, then allowed to incubate in the same M199 media minus serum and insulin for 1 hr prior to stimulation. For probe excitation, the A1Rsi LSCIS utilized the 561 nm diode laser (mCherry), and the 405 nm laser line (Hoechst 33342) to acquire images of the cells by sequential excitation. The mCherry-*Plin5* expressing cells were imaged showing PLIN5 localization at time zero, then treated with 1 mM of the cAMP analog 8-bromoadenosine 3′,5′-cyclic monophosphate and imaged every 10 min for 1.5 hr. Image files were analyzed using NIS-Elements software. For colocalization experiments, NIS-Elements was used to identify mCherry-PLIN5 pixels colocalized with Hoechst 33342. Z stack or multiple focal planes were imaged to ensure compartmentalization and localization.

To determine the molecular association between PLIN5, SIRT1, and PGC-1α in the nucleus, co-localization and FRET analysis was performed by acceptor photobleaching as described previously (McIntosh et al., 2012; Najt et al., 2014; Senthivinayagam et al., 2013). Briefly, primary hepatocytes were co-transfected with mCherry-*Plin*5 (acceptor) and eGFP-*Sirt*1 (donor) or eGFP-*Pgc-1α* (donor). Prior to imaging, cells were washed twice with PBS and placed in M199 media containing 23 mM HEPES, 26 mM sodium bicarbonate, 50 IU/mL penicillin, 50 μg/mL streptomycin, 11 mM glucose, and 1mM carnitine. Digital images were taken under basal

conditions, then the cells were treated with 1 mM 8-bromoadenosine 3′,5′-cyclic monophosphate for 1 h. Images were acquired utilizing the 561 nm diode laser (mCherry) and the 488nm laser (eGFP) to acquire images of the cells by sequential excitation. Co-localization of the two probes was determined as described above. Upon establishing the two probes co-localized, acceptor photobleaching FRET experiments were performed to measure the increase in donor (eGFP) emission upon photobleaching of the acceptor (mCherry) as described elsewhere (McIntosh et al., 2012; Senthivinayagam et al., 2013). To calculate the FRET efficiency (*E*), representing the efficiency of energy transfer between donor and acceptor, the following equation was used: $E = 1\text{-}(I_{DA}/I_D)$ where I_{DA} is donor fluorescence intensity before acceptor photobleaching and I_D is the donor fluorescence intensity after acceptor photobleaching. An average *E* value was calculated from eGFP fluorescence emission increase after photobleaching. The intermolecular distance *R* between PLIN5 and SIRT1 or PLIN5 and PGC-1α was calculated from the equation $E = 1/(1\text{-}(R/R_o)^6)$, where *E* is experimentally determined and R_o is the Foster radius for the eGFP-mCherry FRET pair. For the FRET efficiency images, analysis was performed in MetaMorph 7.5 (Molecular Devices, Sunnyvale, CA). Images were filtered to remove randomized noise by using a low pass filter. The filtered images of the donor emission before acceptor photobleaching were subtracted from the image after acceptor photobleaching. The resultant image was divided by the image of donor emission after acceptor photobleaching and multiplied by 100 to generate bar-scale FRET efficiencies.

Tissue histology

Tissue samples (25-75 mm^3 segments) were fixed in a 10% buffered formalin solution at room temperature overnight, then stored in alcohol until embedded in paraffin, section (4-6 m thickness). Immunohistochemistry was performed as described previously (Najt et al., 2014; Sathyanarayan et al., 2017). Sections were probed with anti-PLIN5 (Progen, Heidelberg Germany), anti-ATGL (CellSignaling Tech, Danvers MA), and anti-PLIN2 (prepared as previously described in (Atshaves et al., 1999)). Histological processing was done at the histopathology laboratory at University of Minnesota. Fluorescent imaging was performed on a Nikon A1Rsi Laser Scanning Confocal Imaging System (LSCIS; Nikon, Melville, NY). H&E slides were imaged on a Leica DM5500B microscope (Leica Microsystems) at 5x-20x magnification.

Western blotting

Cell lysates (30-50 μg protein) were separated on 10%–12% tricine gels using a Mini-Protean II cell (Bio-Rad lab, Hercules, CA) system at constant amperage (30 mA per gel) for about 3 hr. Proteins were then transferred onto PVDF membranes at constant voltage (90 V) for 1.5 hr. Blots were stained with Ponceau S to confirm uniform protein loading (Aldridge et al., 2008; Willenborg et al., 2005) before blocking in 5% BSA in TBST (10 mM Tris-HCl, pH 8, 100 mM NaCl, 0.05% Tween-20) for 1 hr. Blots were incubated with specific poly- or monoclonal antibodies overnight and were developed with IRDye 800CW (LI-COR) or IRDye 680RD (LI-COR) secondary antibodies. To visualize the bands of interest, blots were scanned using the LI-COR Odyssey imaging system (Lincoln, NE). Protein bands were quantitated by densitometric analysis after image acquisition using NIH Scion Image to obtain relative protein levels expressed as integrated density. All values were normalized to β-actin expression or PonceauS staining. Antibodies were purchased or obtained from the following sources; Total-Plin5 (Progen; Heudelberg, Germany), Histone H3, SIRT1, Acetylated Lysine (Cell Signaling Technologies; Danvers, MA), PGC-1α (MilliporeSigma; Burlington, MA), phospho-PLIN5 (NeoBioLab targeting; Cys-LARRGRRW(pS)VELK), PLIN2 [Barbara Atshaves developed in (Atshaves et al., 1999)].

Cellular fractionation

Nuclear and cytoplasmic fractions from mouse tissues were prepared as previously described in (McIntosh et al., 2010; Muratore et al., 2018; Storey et al., 2012). Briefly, livers were excised, minced in homogenate buffer [10 mM Tris-base pH 7.0 with protease (Complete protease inhibitor cocktail, Roche, Basel Switzerland), phosphatase (PhosSTOP, Sigma-Aldrich, St. Louis, MO), and de-acetylase inhibitors (De-acetylase Cocktail, MedChem Express, Monmouth Junction, NJ)], placed in a nitrogen cavitator and charged with nitrogen to 150 psi. The cavitator was submerged in ice allowed to lysis the tissue for 15 min. Liver lysates were harvested and spun at 1,000 x g for 10 min to obtain a post-nuclear supernatant. The pellet from this spin was suspended in nuclear isolation buffer (10 mM Tris-base pH 7.5, 10 mM KCl, 2 mM $MgCl_2$, 1 mM EDTA, 1 mM EGTA, 1 mM DTT, with protease, phosphatase, and acetylase inhibitors). The re-suspended nuclear fraction was spun at 2,000 x g for 20 min, the supernatant was discarded and the pellet that contained nuclei kept. Nuclei were suspended in homogenate buffer described above supplemented with 10 mM KCL and 2 mM $MgCl_2$. The post-nuclear supernatant was loaded onto a sucrose step gradient (4 mL 35% sucrose, 4 mL 25% sucrose) and centrifuged at 36,000 rpm in a Beckman SW41 swinging bucket rotor for 4 hr. The LD fraction appeared as white film at the top of the tube, which was removed with a Pasteur pipette. Both the LD and nuclear fraction from fed and 16 hr fasted mice were snap frozen for latter analysis via western blotting.

PLIN5 structural prediction and analysis

The secondary structure of PLIN5 was predicted by the PredictProtein server https://www.predictprotein.org/. Secondary structural predictions generated by PredictProtein were consistent with further analysis by PSIPRED, SAM, and SABLE2. Similar to methods used to predict the lipid binding domain of PLIN2 (Najt et al., 2014) the PLIN5 C-terminal domain structure was modeled by homology

to the structure of residues 209-431 in PLIN3 from Protein Data Bank entry 1SZ1 by using Modeler, as implemented in the ModWeb Web server (https://modbase.compbio.ucsf.edu/modweb/) and the online webserver Phyre[2] (http://www.sbg.bio.ic.ac.uk/phyre2/html/page.cgi?id=index).

Expression and purification of recombinant proteins in *Escherichia coli* cells

Recombinant PLIN5 was purified using the following procedure. *Plin5* was cloned into pTEV6-HIS-MBP expression construct. Protein was overexpressed in *E. coli* host strains BL21 codon plus* (Agilent, Santa Clara, CA) and grown at 37°C in 1L cultures containing 2XYT sterile fermentation media 100 μg/mL Carbenicillin until OD_{600} = 0.6. Once the desired OD was obtained, the culture was cooled to 18°C and induced with IPTG. After 16 hr, cells were harvested by centrifugation and re-suspended in buffer A (50 mM HEPES, 500 mM NaCl, 10% glycerol, pH 8.0). The re-suspended cells were cracked by sonication. Lysates were clarified by ultra-centrifugation (4°C for 60 min at 48,000 x g). The clarified lysate was applied to a amylose resin column (Thermo, Waltham, MA) equilibrated with buffer A at a flow rate of 0.5 mL/min. The column was washed with 20 column volumes of buffer B (50 mM HEPES, 300 mM NaCl, 10%glcerol 10 mM Maltose pH 8.0) at a flow rate = 1.0 mL/min. The protein was eluted using buffer C (50 mM HEPES, 300 mM NaCl, 250 mM Maltose, pH 8.0; flow rate = 1.0 mL/min) where the purified protein was identified by UV280 signal. The elution pool was diafiltered for 5 diavolumes of buffer D (25 mM HEPES, 100 mM NaCl, 5 mM DTT, 10% glycerol, pH 7.5) and then checked for purity by SDS-page analysis. The purified His-MBP-Plin5 protein was incubated with TEV-protease to cleave the His-MBP tag. The cleaved product was applied to Ni-NTA column and the flow through was collected. Purity of the un-tagged Plin5 protein was determined by SDS-page analysis. For binding and activity assays, purified protein was buffer exchanged to the appropriate buffer using a Ultrcel-50K (EMD Millipore, Darmstadt, Germany).

Recombinant SIRT1 was purified as previously described with some modifications (William C Hallows, Susan Lee, and John Denu, PNAS 2006). Briefly, proteins were overexpressed in *E. coli* host strains BL21 codon plus* (Agilent, Santa Clara, CA) and grown at 37°C in 15L cultures containing 2X YT sterile fermentation media 100 μg/mL Carbenicillin until OD_{600} = 3.0. Once the desired OD was obtained, the culture was cooled to 18°C and induced with IPTG. After 5 h, cells were harvested by centrifugation and re-suspended in buffer A (50 mM HEPES, 300 mM NaCl, 10 mM Imidazole, pH 8.0). The re-suspended cells were cracked by two passes through a microfluidizer (G30Z and H10Z interaction chambers) at 16,500 psi. Lysates were clarified by centrifugation (4°C for 30 min at 15,000 x g) and filtration through a 1μm filter. The clarified lysate was applied to a 20 mL Hispur-Ni2+ column (Thermo, Waltham, MA) equilibrated with buffer A at a flow rate of 5.0 mL/min. The column was washed with 10 column volumes of buffer B (50 mM HEPES, 300 mM NaCl, 20 mM imidazole pH 8.0) at a flow rate = 5.0 mL/min. The protein was eluted using buffer C (50 mM HEPES, 300 mM NaCl, 500 mM imidazole, pH 8.0; flow rate = 8.0 mL/min) where the purified protein was identified by UV280 signal. The elution pool was diafiltered for 5 diavolumes of buffer D (25 mM HEPES, 100 mM NaCl, 5 mM DTT, 10% glycerol, pH 7.5) and then checked for purity by SDS-page analysis. For binding and activity assays, purified protein was buffer exchanged to the appropriate buffer using a Ultrcel-50K (EMD Millipore, Darmstadt, Germany).

Intrinsic tryptophan fluorescence binding studies

The binding of fatty acids to PLIN5 and SIRT1 was examined by measuring the fluorescence quenching of PLIN5 and SIRT1 tryptophan residues after addition of ligand as described previously (Najt et al., 2014). In brief, the intrinsic tryptophan fluorescence of PLIN5 and SIRT1 (150 nM in 10 mM NaH_2PO_4, pH 7.5) was monitored from 300 to 400 nm after excitation at 295 nm (to minimize interference from tyrosine fluorescence) both before and after addition of increasing increments of fatty acids (fatty acids were dissolved in 200 proof spectroscopically clear ethanol) using a Cary Eclipse fluorescence spectrophotometer. Data was corrected for back ground scatter originating from the buffer and ligand without protein present. The intrinsic tryptophan fluorescence in the presence of different concentrations of ligand was plotted as the maximum fluorescence difference ($\Delta F = F_0$-F) versus ligand concentration to yield a saturation curve where F and F_0 were the measured fluorescence emission intensity of the protein solution in the presence and absence of ligand, respectively. The dissociation constant K_d was determined from the double reciprocal plot of the saturation curve. Linear regression of $1/[1-(F/F_{max})]$ versus $[ligand]/(F/F_{max})$ yielded a slope = $1/K_D$ and ordinate intercept = nE_0/K_d where F represented fluorescence intensity at a given concentration of ligand, F_{max} was the maximal fluorescence. E_0 was the protein concentration, and n equaled the number of ligand binding sites.

Circular-Dichroic analysis of secondary structure

The far UV circular dichroic (CD) spectra of each protein was measured in phosphate buffer (10 mM NaH_2PO_4, pH 7.5 with 10 mM NaCl) in the presence and absence of ligand. PLIN5 was assayed at 3 μM and SIRT1 was assayed at 5 μM. Experiments were performed at 25°C in a 1 mm path length crystal cuvette using a JASCO J-815 CD spectrometer (JASCO Analytical Instruments, Easton, MD). Experiments with ligand were allowed to incubate 2-5 min prior to each scan to allow maximal protein-ligand interaction. CD spectra were recorded from 270 to 190 nm at a scan rate of 50 nm/min with a time constant of 1 s and bandwidth of 2 nm. For each experiment, 10 iterations were performed in triplicate. Secondary structure analysis was carried out using the CDSSTR analysis program (Sreerama and Woody, 2000) with results reported as percentages of regular α helices, distorted α -helices, regular β strands, and distorted β strands, turns and unordered structures.

1,8-ANS displacement assays for lipid binding

PLIN5 and SIRT1 lipid binding was measured using a 1-anilinonaphthalene 8-sulfonic acid (1,8-ANS) displacement assay as previously described (Kane and Bernlohr, 1996). 1,8-ANS was dissolved in absolute ethanol and its concentration determined spectrophotometrically (ε_{372} = 8,000cm^{-1}, M^{-1}). Increasing amounts of protein were incubated with 500 nM 1,8-ANS in 50 mM sodium phosphate pH 7.5. The samples were mixed for 1 min under dim light and the fluorescence was measured in a Perkin Elmer 650-10S fluorescence spectrophotomer. Slit widths of 4 nm were used for both excitation and emission. Fluorescence intensity was plotted versus increasing protein concentration to generate a binding curve. Binding parameters were determined using Scatchard analysis. Upon establishing 1,8-ANS binding to PLIN5 and SIRT1, various lipids were assessed for their ability to displace the fluorescent probe. PLIN5 (1 μM) and SIRT1 (2.5 μM) were added to 50 mM sodium phosphate pH 7.5 mixed with 500 nM 1,8-ANS at 25°C and the fluorescence signal determined. Increasing concentrations of competitor lipids were added to the 1,8-ANS-protein complex, allowed to mix for 60 s and the fluorescence signal recorded. The decay in normalized fluorescence as a function of the competitor concentration was used to determine the displacement curve and the I_{50}. The apparent Ki was calculated using $K_i = [I_{50}]/(1+[L]/K_D)$, where K_i is the apparent inhibitor constant, [L] is the free concentration of 1,8-ANS, and the K_D is the apparent dissociation constant of a given protein for 1,8-ANS.

Peptide synthesis and purification

Peptides were synthesized using a Protein Technologies SymphonyX synthesizer and using 4-methylbenzydrylamine hydrochloride resin (Iris Biotech GMBH) (Perez et al., 2019). Standard Fmoc-protected amino acid (AA) coupling occurred in the presence of 95 mM HCTU (Iris Biotech GMBH) and 200 mM N-methylmorpholine (Gyros Protein Technologies; S-1L-NMM) over two 20-min coupling cycles. Fmoc deprotection occurred in the presence 20% piperidine in dimethylformamide (DMF, Iris Biotech GMBH;) over two 5-min cycles. The peptides were purified to > 95% purity by preparative C18 reverse phase HPLC (Agilent 1200 series) over a water/0.1% TFA and acetonitrile/0.1% TFA gradient characterized using HPLC-MS (Agilent 6300 MSD). Peptide substrates were dissolved in mass spectrometry grade water. Absorbance measurements at 280 nm wavelength were used to determine the peptide concentration; peptide extinction coefficients were calculated using ExPASy Bioinformatics Resource portal (https://web.expasy.org/protparam/).

HPLC-MS/MS SIRT1 deacetylation assay

For the deacetylation assay, 1 μM recombinant SIRT1 purified from *E. coli* was incubated with different concentrations of H3K9, PGC-1α, FOXO3a, and p53 acetylated peptides (0-250 μM) and fatty acids in 50 μL reaction mixture (25 mM Tris-base, pH 8.0, 50 mM NaCl, 1 mM DTT, 1 mM NAD$^+$) at 37°C for 60 min. To quench the reactions, 50 μL ice cold acetonitrile was added into the reaction mixture. After centrifuging at 15,000 x g for 15 min, the supernatant was collected, transferred to a clean tube, and blown down under nitrogen. Samples were re-suspended in ultra-high purity MS/MS grade water and analyzed by HPLC-MS/MS Selective Reaction Monitoring (SRM) Analysis. Samples (10 μl) for SRM analysis were subjected to separation using an Shimadzu UFLCXR system coupled to an analytical Waters Acquity BEHc18 column (1.7um particle size, 2.1x50 mm) at 50°C, running a linear gradient of A: 15% acetonitrile/0.55% formic acid, and B: 55% acetonitrile/0.1% formic acid for 12 min at a column flow rate of 400 μl/min. The HPLC was connected to a Applied Biosystem 5500 iontrap fitted with a turbo V electrospray source run in positive mode with declustering potential and collision energies in Table S5. The column was cleared with 95% acetonitrile for 2 min and then equilibrated to buffer A for 3 min. Transitions monitored as in Table S5 were established using the instrument's compound optimization mode with direct injection for each compound. The data was analyzed using MultiQuant software (ABI Sciex Framingham, MA) providing the peak area. A standard curve was constructed using synthetically produced product peptides from picomole to nanomole levels in 10 μl. Samples were run in triplicate and concentrations determined from the standard curve.

Dietary experiments

One week before the start of the feeding experiments, age-matched male (6-8 week old, 20-30 g) inbred C57BL/6 mice obtained from Harlan Laboratories and placed on a control diet containing 15% fat derived primarily from soybean oil and lard (Envigo Teklad custom diet no. TD170820). After 1 week, half of the mice remained on the control diet, whereas the rest were switched to an isocaloric olive oil diet contain 15% fat derived primarily from olive oil (Envigo Teklad custom diet no TD170821). Mice were fed *ad libitum* for 12 weeks. At the end of the feeding study, mice were fasted for 16 h prior to tissue and serum collection. A second cohort of mice were placed on the same dietary regiment as described above with the following modifications; 3 days prior to tissue harvest, half the mice fed the control diet and half the mice fed the olive oil enriched diet were injected IP daily with 10 mg/kg of the SIRT1 inhibitor EX527 while the remaining mice were injected with equivalent amounts of DMSO.

Serum analysis

Non-esterified fatty acid levels in serum were determined using Wako Chemicals lipid assay systems (Wako Diagnostics, Richmond, VA). Colorimetric analyses of lipids were measured at 570 nm on an Omega FLOUstar 96-well plate reader from BMG labtech (Ortenberg, Germany). Serum β-hydroxybutyrate measurements were determined from mouse serum samples using a β-hydroxybutyrate LiquiColor kit (Stanbio Laboratory, Boerne, TX, USA) according to the manufacturer instructions.

Co-immunoprecipitation studies

The Nuclear Complex Co-IP system from Active Motif (Carlsbad, CA) was used for co-immunoprecipitation (co-IP) experiments following the manufacturers' protocol. Briefly, nuclei from primary hepatocytes were isolated. Nuclear fractions were incubated overnight with kit reagents and anti-bodies (anti-acetyl-lysine, anti-FOXO3a, anti-PLIN5, anti-PGC-1α or anti-SIRT1) at 4°C with shaking. The next day, unbound fractions were separated by magnet, followed by washing and elution of the bound complex. Eluate proteins were analyzed by western blotting. A parallel co-IP with the lysates using anti-rabbit IgG was performed to assess nonspecific binding (negative control). Input material was run in parallel to determine equal loading of sample. Immunoprecipitations performed to determine protein acetylation were carried out as described previously in (Khan et al., 2015).

cAMP-Glo Assay

The cAMP-Glo Assay from Promega (Promega, Fitchburg, WI) was used for cAMP detection according to the manufactures protocol. MEF cells were plated in a 96-well plate in complete media (DMEM 10% FBS, 1%P/S). Cells were treated for 6 or 16 hr with 2% fatty acid free BSA or 500 μM 18:1 complexed to fatty acid free BSA. After being treated with complexed fatty acids, cells were washed 2x with PBS, then placed in fasting media (DMEM, 0.5% P/S) and treated with DMSO or 20 μM isoproterenol/500 μM IBMX for 20 min. Cells were lysed with cAMP-Glo lysis buffer at room temperature for 15 min. Cell lysate was treated with cAMP Detection Solution, mixed and incubated at room temperature for 20 min. The reaction was then treated with Kinase-Glo Reagent, mixed for 60 s and incubated at room temperature for 10 min. Luminescence was then read on a Cary Eclipse fluorescence spectrophotometer (Agilent, Santa Clara, CA).

QUANTIFICATION AND STATISTICAL ANALYSIS

Values were expressed as the means ± SEM. In comparisons made between two groups, Student's t tests were performed using Graphpad Prism (San Diego, CA). When more than two groups were compared, analysis of variance (ANOVA) with Newman Keuls post hoc test were performed. Values with $p < 0.05$ were considered statistically significant.

DATA AND CODE AVAILABILITY

This study did not generate any unique dataset or code.

Molecular Cell, Volume *77*

Supplemental Information

Lipid Droplet-Derived Monounsaturated Fatty Acids Traffic via PLIN5 to Allosterically Activate SIRT1

Charles P. Najt, Salmaan A. Khan, Timothy D. Heden, Bruce A. Witthuhn, Minervo Perez, Jason L. Heier, Linnea E. Mead, Mallory P. Franklin, Kenneth K. Karanja, Mark J. Graham, Mara T. Mashek, David A. Bernlohr, Laurie Parker, Lisa S. Chow, and Douglas G. Mashek

Supplemental Figure 1

A

CO_2-KQTARKSTGGWWK-NH_2	H3K9
CO_2-KQTARK(Ac)STGGWWK-NH_2	H3K9-Acetylated
CO_2-KNSWSNETKVIAPNT-NH_2	PGC-1αK183
CO_2-KNSWSNETK(Ac)VIAPNT-NH_2	PGC-1αK183-Acetylated
CO_2-KDSPSQLSKWPGSPTS-NH_2	FOXO3aK290
CO_2-KDSPSQLSK(Ac)WPGSPTS-NH_2	FOXO3aK290-Acetylated
CO_2-KWEEKGQSTSSHSKNSTEGAEE- NH_2	p53
CO_2-KWEEKGQSTSSHSK(Ac)NSTEGAEE- NH_2	p53-Acetylated
CO_2-KWEEKGQSTSSHSKNSTEGWEE- NH_2	p53-W
CO_2-KWEEKGQSTSSHSK(Ac)NSTEGWEE- NH_2	p53-W-Acetylated

B

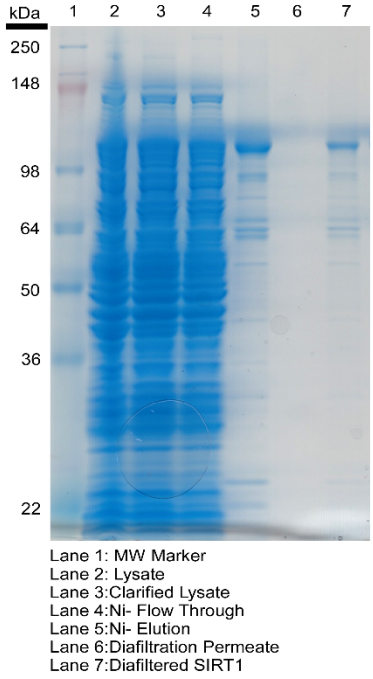

C

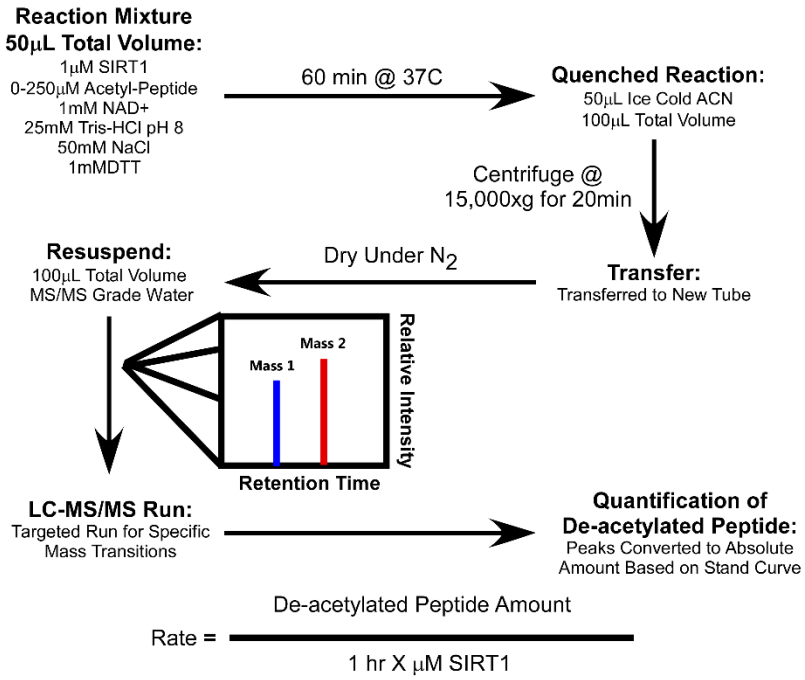

D

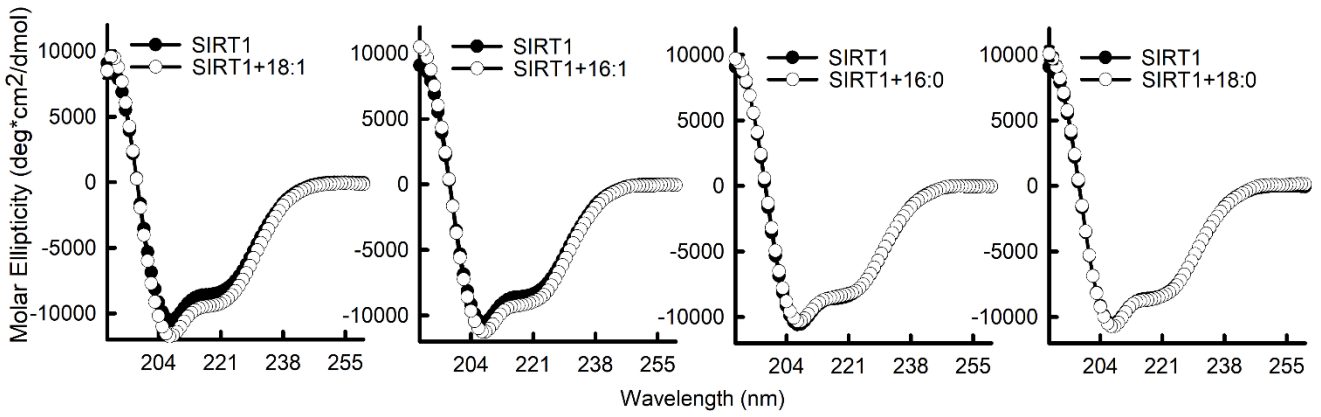

Fig. S1 (Related to Figure 1-2 and Figure S4). A) Peptide sequences for acetylated and de-acetylated SIRT1 protein targets H3, PGC-1α, p53 wild-type, p53-W mutant, and FOXO3a. Peptides were synthesized using a Protein Technologies SymphonyX synthesizer as described in the methods. The peptides were purified to >95% purity by preparative C18 reverse phase HPLC (Agilent 1200 series) over an acetonitrile/0.1% TFA and water/0.1% TFA gradient and characterized using HPLC-MS (Agilent 6300 MSD). Purity was determined by absorbance spectra at 214 nm and 280 nm and by mass spectrometry.

B) Recombinant full length SIRT1 protein on a 10% Tricine-PAGE gel. C) Workflow for the SIRT1 deacetylase assay. The deacetylation reaction was carried out as shown and as described in the supplemental methods section. Mathematical formula for determining SIRT1 deacetylation rate.
D) Circular dichroic analysis of SIRT1. Far ultraviolet (UV) circular dichroic (CD) spectra of SIRT1 shown in the presence or absence of ligands. Each spectrum represents an average of 10 scans repeated in triplicate.

Supplemental Figure 2

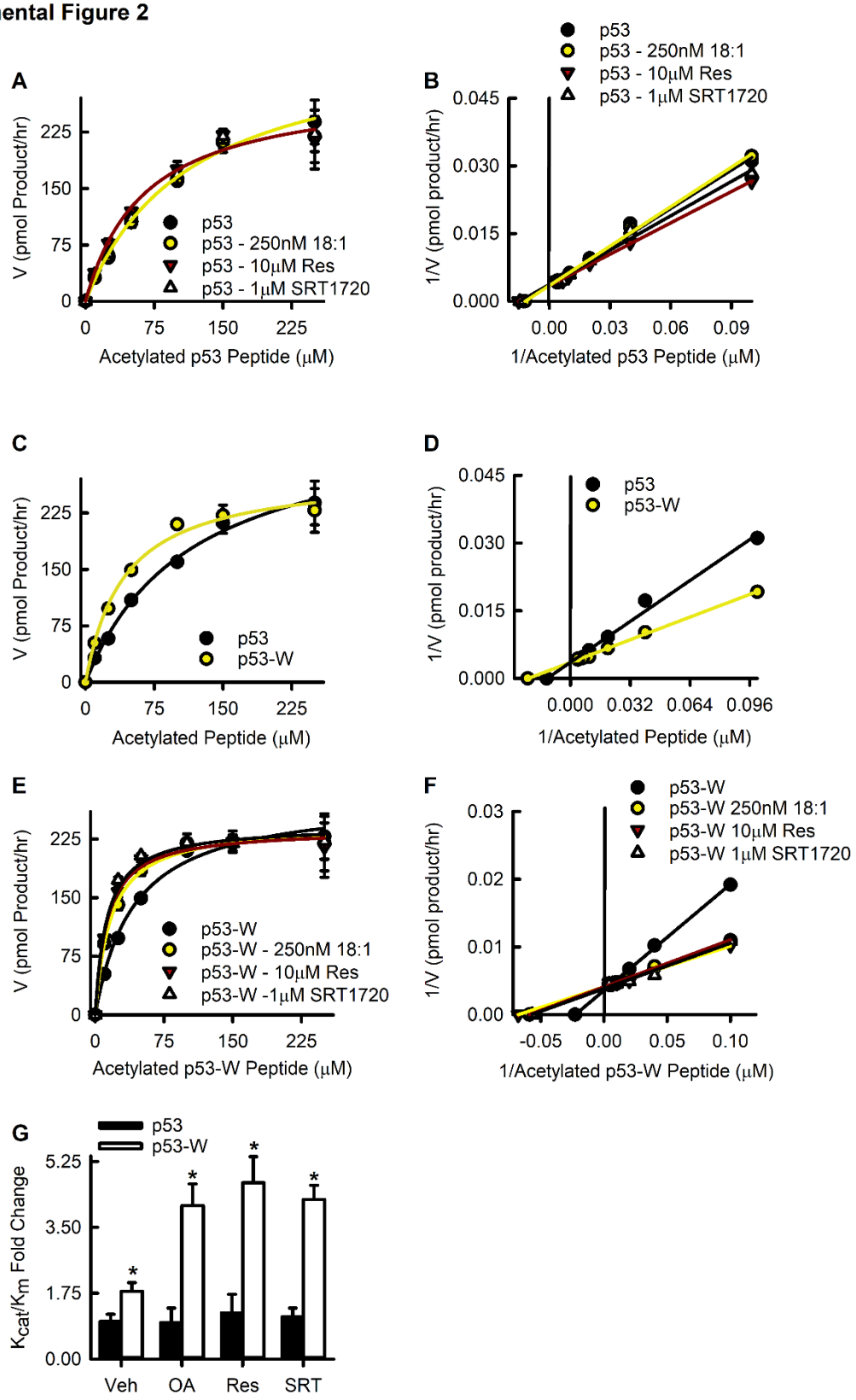

Fig. S2 (Related to Figure 1-2). A) Saturation plot of SIRT1 activity towards wild-type p53 in the presence of veh, 250 nM 18:1 fatty acid, 10 μM resveratrol (Res), or 1 μM SIRT1 activating compound SRT1720. B) Lineweaver-Burk reciprocal plots were generated to determined. C) Saturation plot of SIRT1 towards wild-type p53 and the p53-W mutant. D) Lineweaver-Burk plots based with the two p53 peptides. E) Saturation plot of SIRT1 activity towards mutant p53-W in the presence of veh, 250 nM 18:1

fatty acid, 10 μM resveratrol (Res), or 1 μM SIRT1 activating compound SRT1720. F) Lineweaver-Burk reciprocal plots were generated to determine K_m, V_{max}, and K_{cat} for SIRT1 towards wild-type p53 and mutant p53-W. G) K_{cat}/K_m fold change for wild-type p53 and mutant p53-W in the presence of veh, 250 nM 18:1 fatty acid, 10 μM resveratrol (Res), or 1 μM SIRT1 activating compound SRT1720. * $p<0.05$ vs. veh, $^{\#}p<0.05$ vs. wild-type p53.

Supplemental Figure 3

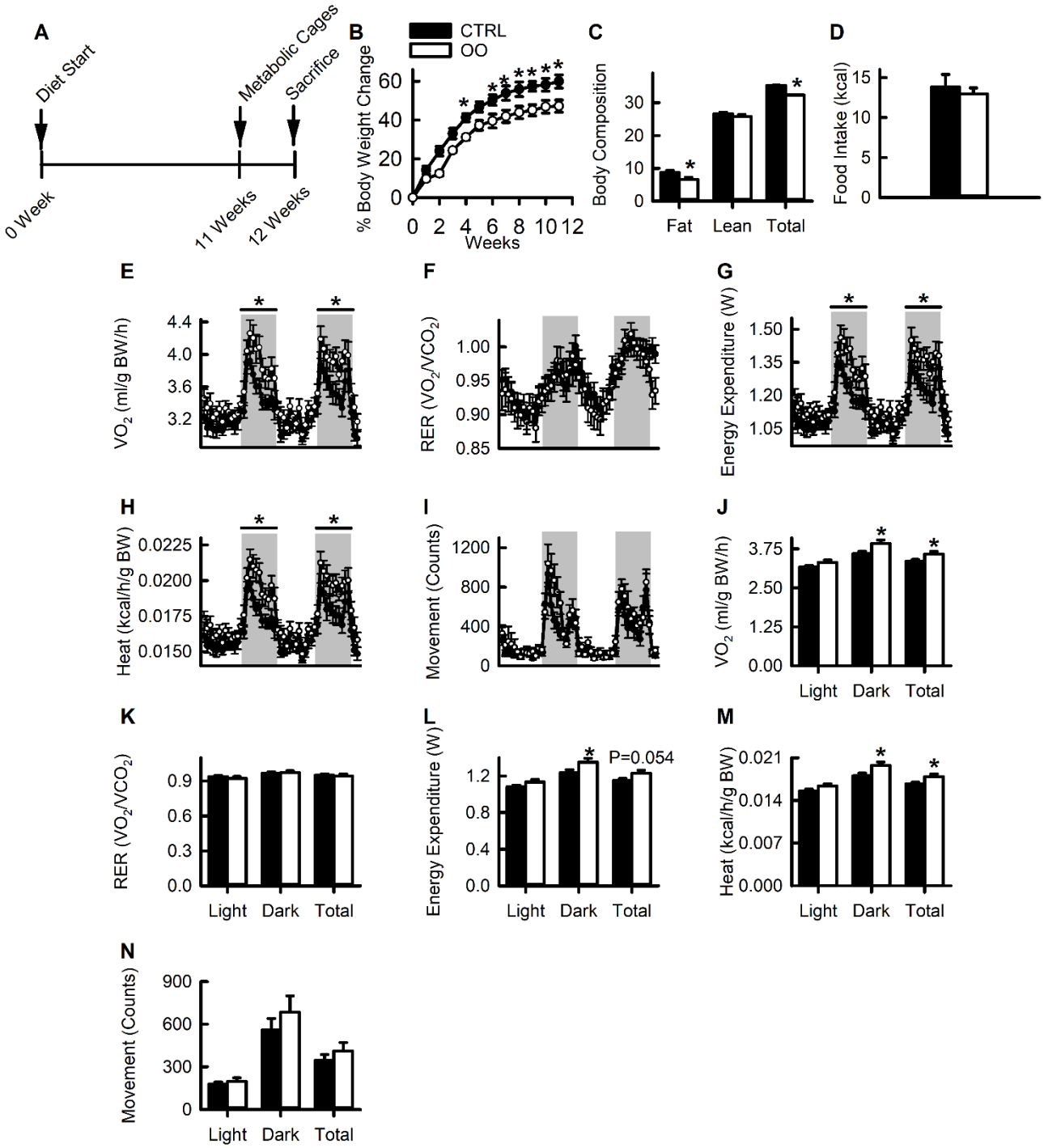

Fig. S3 (Related to Figure 4). A) Workflow for the mice fed CTRL or OO diets. B) Percent body weight change was determined for mice fed the CTRL or OO diets for 12 weeks. C) Body composition of mice prior to being placed in metabolic cages (11 weeks on the diet). D) Food intake of the mice averaged over the course of 12 weeks. E-I) Indirect colometry was used to determine energy balance of mice fed a CTRL or OO diet. Mice were placed in metabolic cages and allowed to acclimate for 24 hrs prior to data collection. J-N) Area under the curve was determined for light and dark cycles (white area=day; grey area=night). N=6 per group. * $p<0.05$ vs CTRL diet.

Supplemental Figure 4

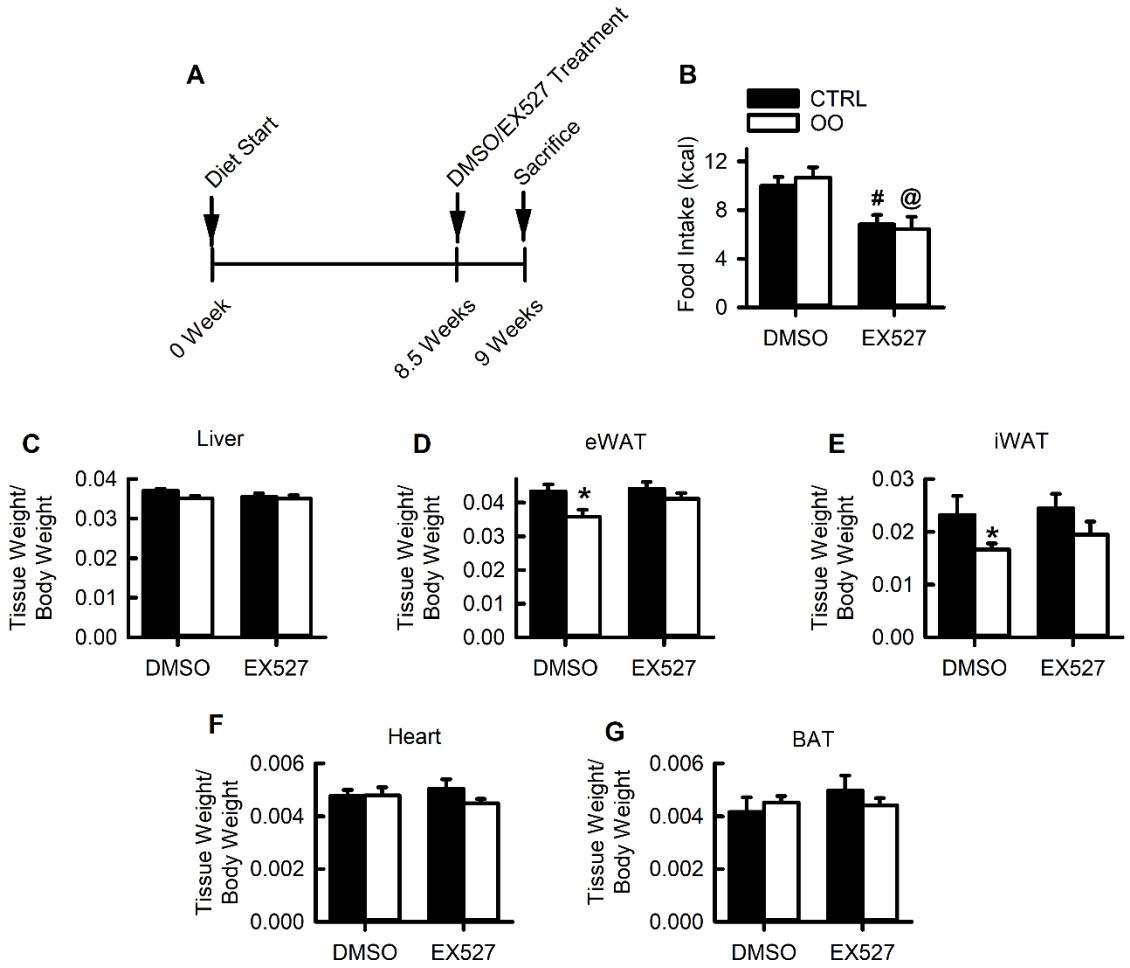

Fig. S4 (Related to Figure 4). A) Workflow for CTRL or OO fed mice treated with DMSO or EX527 (10 mg/kg). B) Food intake was determined for the 8 weeks of diet feeding and EX527 treatment. C-G) Tissue weight per body weight was calculated post sacrifice. N=6-12. *P<0.05 vs CTRL.

Supplemental Figure 5

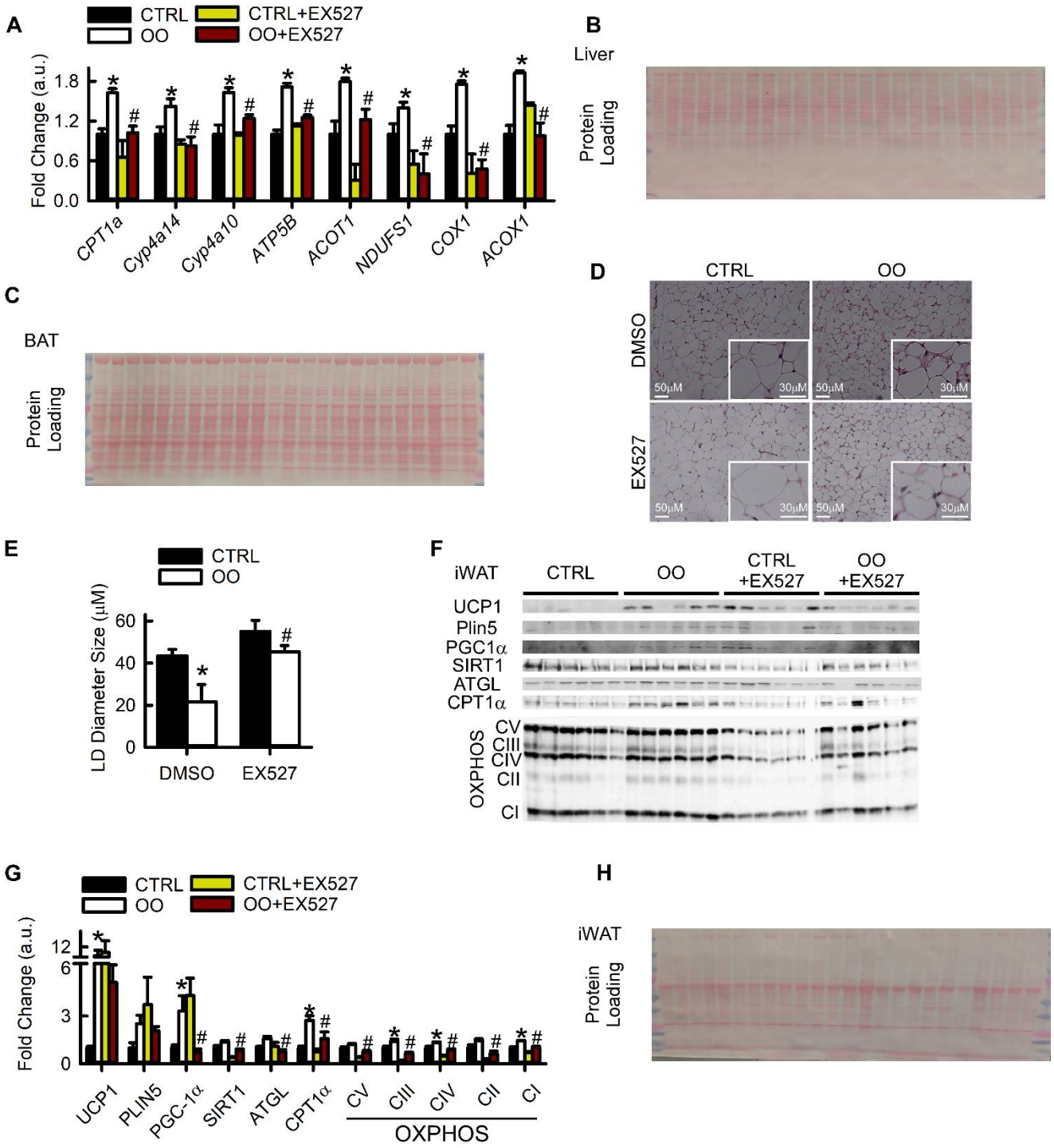

Fig. S5 (Related to Figure 4). A) Expression levels of hepatic PGC-1α/PPAR-α target genes (n=8). B-C) Protein loading for Western blot analysis of tissue lysates as determined by Ponceau S staining; 30-50 μg protein were loaded. D-E) H&E staining of inguinal white adipose tissue (iWAT) from CTRL and OO fed mice. LD size was determined using 3-4 images from 2-3 mice per group. F-G) Relative protein expression levels of UCP1, PLIN5, PGC-1α, SIRT1, ATGL, CPT1α, and OXPHOS complex CI-V in iWAT were determined by Western blotting and quantified by densitometric analysis. H) Protein loading for Western blot analysis of tissue lysates as determined by Ponceau S staining. 30 μg protein loaded. *$p<0.05$ vs. CTRL diet, $^{\#}p<0.05$ vs. DMSO.

Supplemental Figure 6

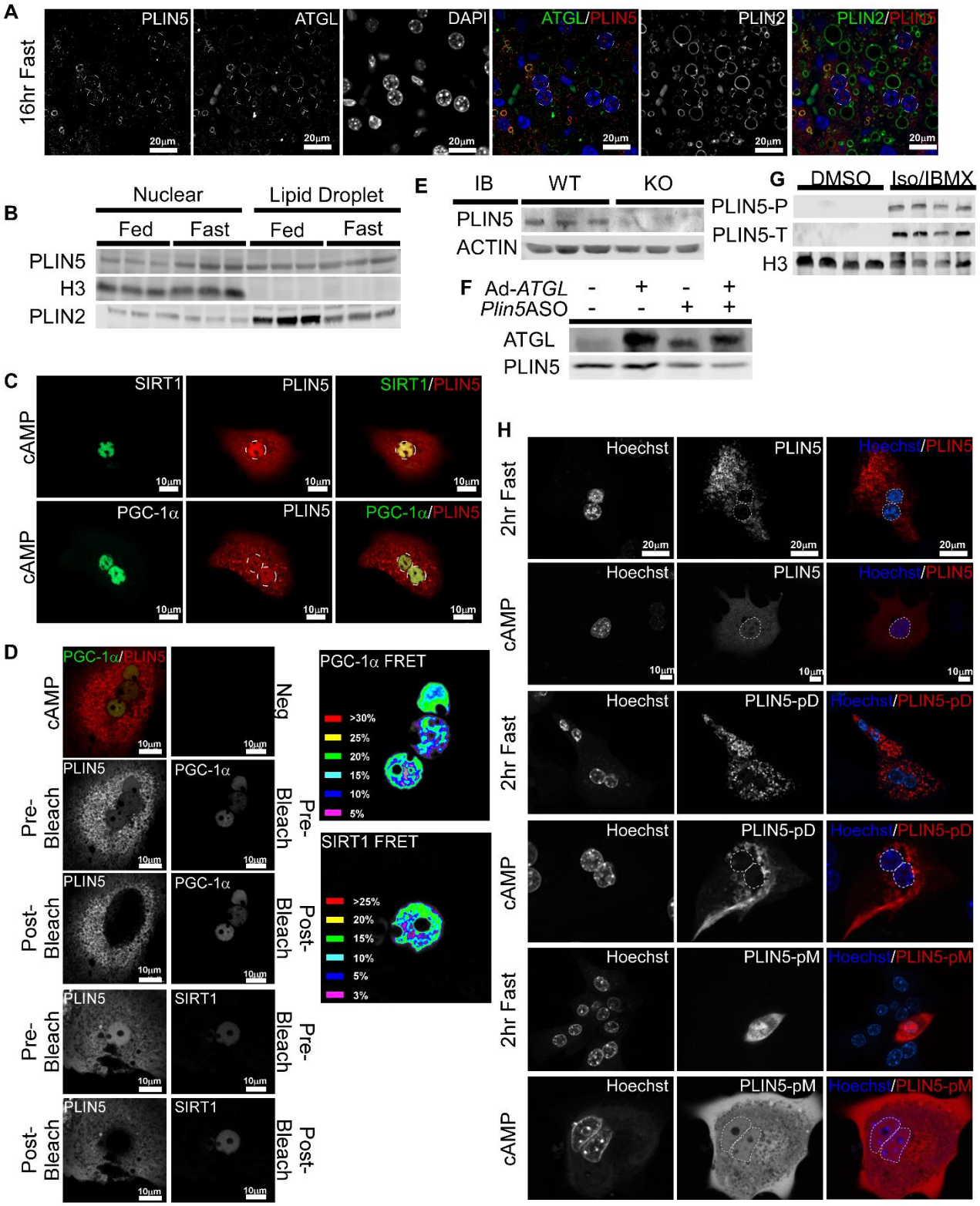

Fig. S6 (Related to Figure 5). A) Confocal imaging of liver sections immunostained with anti-PLIN5, anti-ATGL, and anti-PLIN2 antibodies reveal that ATGL and PLIN5 co-localize to small LDs (n=2-3). B) Livers from fed and 16 hr fasted mice were harvested and subjected to organelle isolation (n=3 mice). C) Co-transfection of primary hepatocytes with eGFP-*Sirt1*/mCherry-*Plin5* or eGPF-*Pgc-1α*/mCherry-*Plin5* were imaged 60 min post cAMP. D) Co-localization and FRET analysis were performed by acceptor

photobleaching. The FRET overlay was pseudo-colored to visualize regions of higher and lower FRET as shown by the inset color scale; neg=negative control (carried out on 2-3 mouse hepatocyte isolation). E) Western blotting for PLIN5 protein was performed on control L-Cells and *Plin5* knockout cells (n=3). F) Western blotting of liver homogenates from mice treated with control or *Plin5* ASOs and *Gfp* or *Atgl* overexpression adenoviruses and control (n=3). G) Hep3B cells treated with vehicle or a cocktail of isoproterenol and IBMX (10 μM and 500 μM, respectively) for 2 hrs were harvested and then subjected to nuclear isolation and immunoblotting for total PLIN5 and phospho-PLIN5 (targeted towards a phosphorylated human S140) (n=4). H) Primary mouse hepatocytes transfected with mCherry-*Plin5*, *Plin5*-pD, or *Plin5*-pM were treated with veh or cAMP (experiments were performed on 3-4 mouse hepatocyte isolations).

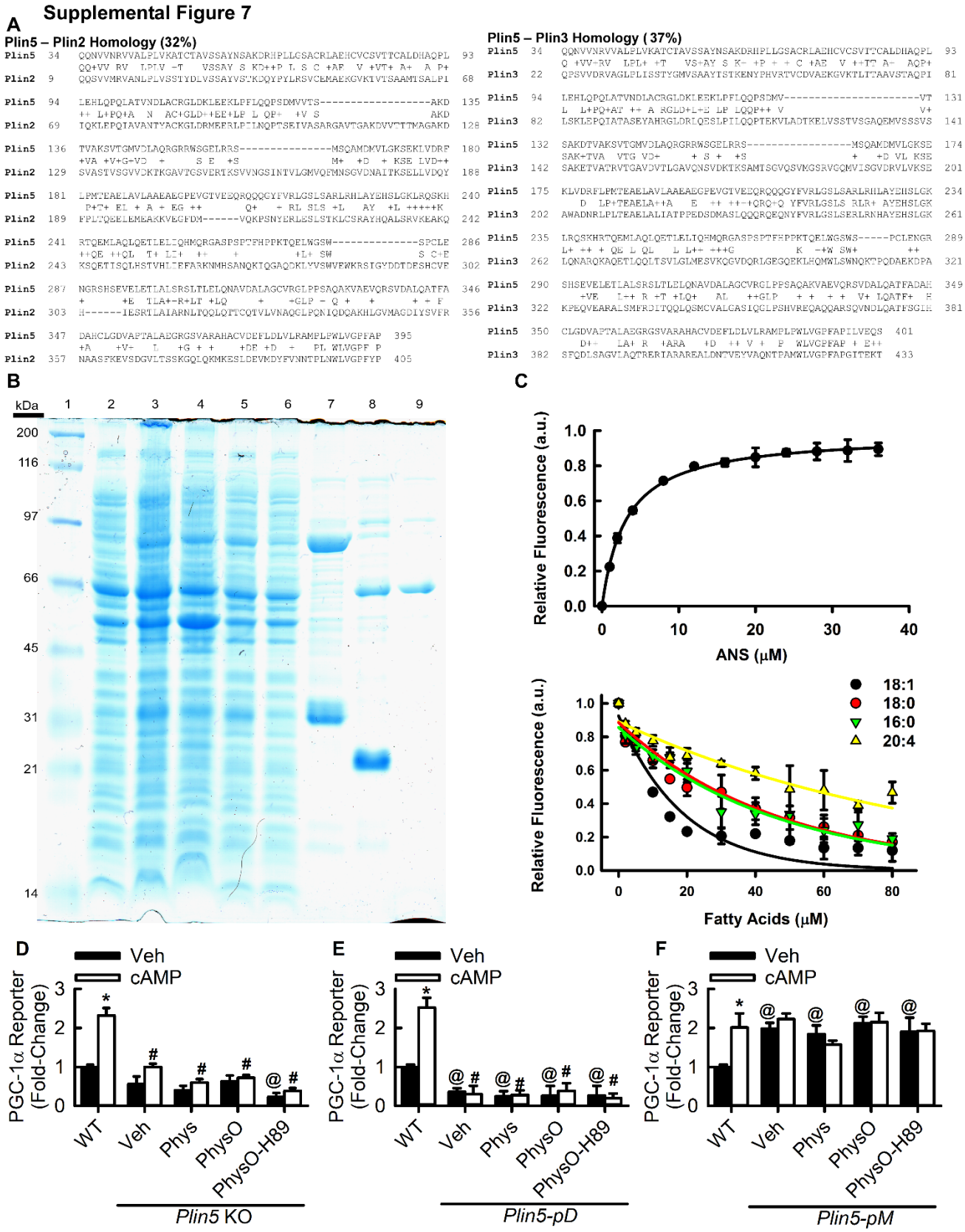

Fig. S7 (Related to Figure 5-6). A) Mouse PLIN5 was aligned with mouse PLIN2 and PLIN3. PLIN5 shared 32% sequence identity with PLIN2 and 37% identity with PLIN3. In the C-terminal region PLIN5 shared 40% sequence identity with PLIN2 and 42% identity with PLIN3. B) Purification of recombinant full length PLIN5 protein was shown on a 10% Tricine-PAGE gel. C) 1,8-ANS binding to PLIN5 and

displacement of 1,8-ANS by fatty acids (n=4-5). D) PGC-1α reporter assays from wild-type and *Plin5* knockout cells (n=6-12). Cells were loaded with a physiological mix of fatty acids lacking 18:1 (Phys), or a physiological mix enriched in 18:1 (PhysO). PKA inhibitor H89 (15 μM) for 1 hr followed by addition of 8-bromoadenosine 3',5'-cyclic monophosphate (cAMP; 1 mM). *$p<0.05$ vs. veh, $^{\#}p<0.05$ vs. wild-type cells, $^{@}p<0.05$ vs. PhysO. E-F) PGC-1α reporter assays in wild-type or *Plin5* knockout cells transfected with the *Plin5-pD* or *Plin5-pM* plasmids (n=6-12). *$p<0.05$ vs. veh, $^{\#}p<0.05$ vs. wild-type cells, $^{@}P<0.05$ vs. wild-type cells without cAMP.

SUPPLEMENTAL TABLES

Table S1. (Related to Figure 1) Fatty acid and resveratrol displacement of 1,8-ANS from SIRT1.

	ANS (K_d)	Ligand	K_i (μM)
SIRT1	31.6 ± 5.6 μM	18:1	5.6 ± 0.12
		16:1	12.5 ± 0.06
		Resveratrol	16.7 ± 0.04
		18:0	ND
		16:0	ND

The dissociation constant (K_d) of SIRT1 and the inhibitory dissociation constant for 1,8-ANS were determined using a fluorescent binding assay as described in the Materials and Methods section. Values represent the mean ± SE (n = 3−4). ND, not detected.

Table S2. (Related to Figure 1 and Figure S1) Predicted secondary structures of SIRT1 in the presence of fatty acids.

		H(r)	*H(d)*	*S(r)*	*S(d)*	*turns*	*unrd*
SIRT1	**- FA**	13.3 ± 0.1	10.55 ± 0.09	9.5 ± 0.2	6.68 ± 0.08	15.9 ± 0.3	43.9 ± 0.6
	+ 16:0	13.0 ± 0.2	10.3 ± 0.2	10.1 ± 0.4	6.9 ± 0.1	16.1 ± 0.2	43.2 ± 0.5
	+ 16:1	14.6 ± 0.5*	11.3 ± 0.6	9.6 ± 0.4	6.53 ± 0.09	15.6 ± 0.4	43 ± 1
	+ 18:0	13.3 ± 0.4	10.5 ± 0.2	10.2 ± 0.4	6.9 ± 0.1	15.9 ± 0.1	42.9 ± 0.2
	+ 18:1	15.9 ± 0.1*	12.7 ± 0.2*	8.3 ± 0.2*	5.9 ± 0.1*	15.7 ± 0.2	41.9 ± 0.5
	+ T18:1	11.9 ± 0.6*	9.8 ± 0.3*	10.8 ± 0.8	7.2 ± 0.4	16.2 ± 0.3	43.4 ± 0.8

Values represent the mean ± SE (10 iterations/run performed in triplicate), n = 3 analyzed by CDSSTR. H(r) indicates regular α-helices; H(d), distorted α-helices; S(r), regular β-sheets; S(d), distorted β-sheets; Unrd, unordered structures. *p≤0.05 vs. no ligand.

Table S3. (Related to Figure 3 and Figure S7) Physiological fatty acid mix for lipid loading and composition of the experimental diets.

Fatty Acid	Carbon	Phys Mix (molarity)	Phys Mix+18:1 (molarity)
Palmitic	C16:0	37	24
Palmitoleate	C16:1	3	2
Stearic	C18:0	12	8
Oleic	C18:1	0	35
Linoleic	C18:2	37	24
Arachidonic	C20:4	9	6
EPA	C22:6	2	1

Fatty acids (500 μM) were complexed BSA (3:1 molar ratio) prior to being added to the cells in culture for 16 hrs.

Table S4. (Related to Figure 4) Composition of the experimental diets.

%Kcal		CTRL	OO
Protein		**18%**	**18%**
	Casein	17.7%	17.7%
	L-Cysteine	0.3%	0.3%
Carbohydrate		**67%**	**67%**
	Sucrose	20%	20%
	Corn Starch	25%	25%
	Maltodextrin	20%	20%
	Fiber	2%	2%
Fat		**15%**	**15%**
	Soybean Oil	9%	4%
	Lard	5%	0%
	Olive Oil	0%	10%
	Fish Oil	1%	1%

Control (CTRL) and olive oil enriched (OO) diets purchased from Envigo; TD-170820 and TD-170821.

Table S5. (Related to Figure 5 and Figure S6) Intracellular targeting and FRET analysis of PLIN5, SIRT1, and PGC-1α in primary hepatocytes.

Protein - Protein	***E* (%)**	***R* (Å)**
PLIN5 – PGC-1α	25 ± 5	67 ± 4
PLIN5 – SIRT1	15 ± 6	73 ± 3

Intracellular targeting, FRET efficiencies *E*, and distance *R* between mCherry-PLIN5 and eGFP-PGC-1α or eGFP-SIRT1 were determined as described in the Materials and Methods section. Values reflect mean ± SE from n=5-6 cells.

Table S6. (Related to Figure 6 and Figure S7) Fatty acid displacement of 1,8-ANS from PLIN5.

	ANS (K_d)	Ligand	K_i (μM)
PLIN5	9.3 ± 1.6 μM	18:1	5.0 ± 0.13
		16:1	9.9 ± 0.07
		18:0	17.7 ± 0.04
		20:4	44.9 ± 0.02

The dissociation constant (K_d) of PLIN5 and the inhibitory dissociation constant for 1,8-ANS were determined using a fluorescent binding assay as described in the Materials and Methods section. Values represent the mean ± SE (n=3−4).

Table S7 (Related to Figure 6). Predicted secondary structures of PLIN5-pD and pPLIN5-pM in the absence or presence of 18:1.

		H(r)	***H(d)***	***S(r)***	***S(d)***	***turns***	***unrd***
PLIN5-pD	**- 18:1**	19.4 ± 0.1	22.5 ± 0.4	7.8 ± 0.1	7.3± 0.1	15.2 ± 0.3	27.7 ± 0.4
	+ 18:1	19.4 ± 0.3	21.5 ± 0.2	10.8 ± 0.2*	7.1 ± 0.2	16.3 ± 0.1*	25.5± 0.2*
PLIN5-pM	**- 18:1**	11.4 ± 0.2*	10.0 ± 0.8*	18.4 ± 0.1*	9.6 ± 0.1*	18.7 ± 0.2*	31.1 ± 0.3*
	+ 18:1	21.4 ± 0.1$^{\#}$	18.3 ± 0.2$^{\#}$	8.1 ± 0.3$^{\#}$	12.8 ± 0.2$^{\#}$	21.8 ± 0.2$^{\#}$	17.7 ± 0.1$^{\#}$

Values represent the mean ± SE (10 iterations/run performed in triplicate), n=3 analyzed by CDSSTR. H(r) indicates regular α-helices; H(d), distorted α-helices; S(r), regular β-sheets; S(d), distorted β-sheets; Unrd, unordered structures. *$p \leq 0.05$ vs. PLIN5-pD; $^{\#}p \leq 0.05$ vs. -18:1.